JGR Space Physics

RESEARCH ARTICLE
10.1029/2023JA032145

Large-Scale Traveling Ionospheric Disturbances Over the European Sector During the Geomagnetic Storm on March 23–24, 2023: Energy Deposition in the Source Regions and the Propagation Characteristics

Grzegorz Nykiel[1,2], Arthur Ferreira[1], Florian Günzkofer[1], Pelin Iochem[1], Samira Tasnim[1], and Hiroatsu Sato[1]

[1]Institute for Solar-Terrestrial Physics, German Aerospace Center (DLR), Neustrelitz, Germany, [2]Faculty of Civil and Environmental Engineering, Gdansk University of Technology, Gdansk, Poland

Key Points:

- Multiple day-time and night-time LSTIDs are triggered at the high latitudes and propagated over Europe down to 35 N on March 23–24, 2023
- We evaluate source energy deposition of LSTIDs from Joule heating and particle precipitation using TEC and incoherent scatter radar data
- Joule heating has more contribution to LSTID generation than particle precipitation during night-time compared to day-time

Supporting Information:

Supporting Information may be found in the online version of this article.

Correspondence to:

G. Nykiel and H. Sato,
grzegorz.nykiel@pg.edu.pl;
hiroatsu.sato@dlr.de

Citation:

Nykiel, G., Ferreira, A., Günzkofer, F., Iochem, P., Tasnim, S., & Sato, H. (2024). Large-Scale Traveling Ionospheric Disturbances over the European sector during the geomagnetic storm on March 23–24, 2023: Energy deposition in the source regions and the propagation characteristics. *Journal of Geophysical Research: Space Physics*, *129*, e2023JA032145. https://doi.org/10.1029/2023JA032145

Received 11 OCT 2023
Accepted 18 FEB 2024

Author Contributions:

Conceptualization: Grzegorz Nykiel, Hiroatsu Sato
Formal analysis: Grzegorz Nykiel, Arthur Ferreira, Florian Günzkofer, Samira Tasnim
Investigation: Grzegorz Nykiel, Arthur Ferreira, Florian Günzkofer, Pelin Iochem, Samira Tasnim, Hiroatsu Sato
Methodology: Grzegorz Nykiel, Florian Günzkofer, Hiroatsu Sato
Visualization: Grzegorz Nykiel

Abstract Multiple Large-Scale Traveling Ionospheric Disturbances (LSTIDs) are observed in the European sector in both day-time and night-time during the magnetic storm on March 23–24, 2023. The Total Electron Content (TEC) observation from a network of GNSS receivers shows the propagation of LSTIDs with amplitudes between around 0.5 and 1 TECU originating from auroral and polar cusp regions down to southern Europe (35°N) with velocities between around 500 and 1,600 [m/s]. We study the energy deposition to the LSTIDs in the source regions and the resulting horizontal propagation over storm-time background density by using continuous measurements of EISCAT incoherent scatter radars in northern Norway and Svalbard that allow for estimating the source energy to the thermosphere-ionosphere system via Joule heating and particle precipitation. Both EISCAT and GNSS TEC data show that the electron density decreased to 50% in the auroral zone after the storm onset. The ionospheric heating caused a nearly 250% increase in the electron temperature above 200 km altitude and the ion temperature above 100 km altitude. We find that Joule Heating acts as a primary energy source for the night-time LSTIDs triggered in the auroral region, while the day-time LSTIDs can be also driven by precipitating particles in the polar cusp. We also find that a significant background density decrease over the whole European sector is caused by this storm for the following day, during which almost no clear LSTIDs are observed.

1. Introduction

Magnetic disturbances in near geospace can trigger Large-Scale Traveling Ionospheric Disturbances (LSTIDs), oscillations of ionospheric density that often originate at high latitudes and travel down to middle and low latitudes with a typical velocity of hundreds of meters per second. Characteristics of the horizontal propagation of LSTIDs have been widely studied. A statistical study using two-dimensional observation of total electron contents (TEC) over Japan shows that the LSTIDs have typical wavelengths (∼ a few thousand kilometers) and oscillation period (∼ a few hours), and the waves become generally damped as they propagate toward lower latitudes (Tsugawa et al., 2004). Although such statistical propagation characterizes can be generally applied to LSTIDs in other longitudinal regions such as in North America (e.g., Ding et al., 2008), individual LSTIDs can have different propagation parameters which could be related to their source mechanisms and storm phase conditions (Borries et al., 2016). Inter-hemispheric propagation was also observed for very large LSTIDs generated in the auroral region (Zakharenkova et al., 2016).

LSTIDs that travel equatorward are considered to be one of the main energy transport mechanisms from source regions at high latitudes toward lower latitudes. Energy sources such as Joule heating and particle precipitations can lead to enhanced thermosphere heating that generates atmospheric gravity waves propagation horizontally away from the source regions. Numerical simulation shows that the gravity waves can be triggered by temperature gradients from various sources, and Joule heating is suggested to be most capable of driving LSTIDs traveling toward lower latitudes from the auroral zone (Richmond, 1979). The varying structure of the thermospheric temperature can influence the vertically generated atmospheric waves through upward reflection, and only fast and large-scale disturbances are allowed to propagate further from the source regions (Richmond, 1978).

Determining primary energy inputs in the ionosphere-thermosphere system and its link to individual LSTID propagation is still observationally challenging. Recent studies combine GNSS TEC and airglow measurements

Writing – original draft: Grzegorz Nykiel, Hiroatsu Sato
Writing – review & editing: Hiroatsu Sato

to show horizontal propagation and source locations of day-time and night-time LSTIDs during magnetic storms. Using a network of airglow imagers in Canada, Lyons et al. (2019) demonstrated individual correspondences of the propagation of night-time LSTIDs in the US sector and auroral disturbance as its source. Nishimura et al. (2020) determined that the source region of dayside LSTIDs is the cusp region, and electron precipitation and Joule heating have been suggested to explain the equatorward-propagating of LSTIDs.

While airglow data provide horizontal information on auroral energy in the source regions of the LSTIDs, an estimate of energy transport in the ionospheric plasma require the precise measurement of electron density and temperature. Incoherent scatter (IS) radar measurement of vertical information of ionospheric plasma is best suited for this purpose. EISCAT IS radar measurements of electron density have been used to study the propagation characteristics of LSTIDs (Cai et al., 2011; Ma et al., 1998) as well as Medium-Scale TIDs (MSTIDs), which are often forced by upward-propagating gravity waves (Günzkofer et al., 2023; Hocke & Schlegel, 1996; Kirchengast et al., 1996; Vlasov et al., 2011). Other forcing mechanisms include interhemispheric electrodynamic coupling along magnetic field lines (Otsuka et al., 2004; Shiokawa et al., 2005; Tsunoda & Cosgrove, 2001) and storm time electric fields which can force TIDs electrodynamically, for example, via the Perkins instability (Kelley et al., 2023; Tsugawa et al., 2007; Zhang et al., 2019, 2022). IS radar can also measure the oscillation period and the vertical wavelength associated with generated gravity waves with high accuracy. If covering whole storm periods, the simultaneous observation of IS radar and TEC imaging may allow for a detailed and systematic study of energy transfer from deposit to propagation and dissipation throughout magnetic storms. An earlier study by van de Kamp et al. (2014) used this approach to study MSTID propagation using GPS data that partially covered Scandinavia and showed that a highly dense network of GNSS receivers covering the EISCAT region is necessary to fully determine the source-propagation relation of TIDs. In order to study the energy source of LSTID generation using this method, continuous observations of IS radars and TEC are required for day and night time during a large magnetic storm.

In this paper, we present an observational study of ionospheric disturbance caused by the geomagnetic storm on 23–24 March 2023, over the European sector and systematically analyze energy depositions to LSTIDs for both day-time and night-time in the source regions. We use a network of GNSS receivers to produce two-dimensional TEC imaging to derive the propagation characteristics. Continuous data sets from EISCAT radars in auroral and polar cusp regions over the storm period are used to accurately measure the density and temperature impact in the source region of LSTIDs and determine the energy deposition levels from Joule heating and particle precision that can generate gravity waves. We also show that the heating of ionospheric density caused a significant decrease in background electron density that also propagated as the geomagnetic disturbances developed.

2. Data and Methodology

2.1. GNSS Data and Processing

The state of the ionospheric density results in the delay and attenuation of GNSS radio signals. In the case of severe geomagnetic storms, GNSS signals can be so delayed/suppressed that accurate positioning becomes challenging (Jacobsen & Andalsvik, 2016; Marques et al., 2018; Poniatowski & Nykiel, 2020). Since the received GNSS signals contain information about the ionospheric delay, they can be used to reproduce the ionospheric conditions. For this purpose, dual-frequency observations can be used to obtain TEC values along the receiver-satellite path (Mannucci et al., 1998):

$$L_I = L_1 - L_2 = -k \cdot STEC + B_s + B_r - N_1 + N_2 + \epsilon \quad (1)$$

where L_I is the so-called geometry-free linear combination of dual frequency carrier phase observations L_1 and L_2. $STEC$ denotes slant TEC: the electron density integrated along the signal path from the satellite to the receiver. B_s and B_r are inter-frequency biases for satellite s and receiver r, respectively. N_1 and N_2 are phase ambiguities, and ϵ denotes other errors like noise or multipath. STEC can be converted to the vertical value ($VTEC$) using the mapping function (Schaer, 1999).

The LSTID can be observed as variations/fluctuations in VTEC. They can be represented by the Rate of TEC (ROT) parameter which, for each time step t, is estimated as a difference between two consecutive VTEC values divided by the sampling interval (Δt):

$$ROT(t) = \frac{VTEC(t) - VTEC(t-1)}{\Delta t} \quad (2)$$

VTEC is measured in TECU (1 TECU = 10^{16}[$electrons/m^2$]). In this study, we also used the Rate of TEC Index (*ROTI*), which is commonly used to estimate the level of the ionospheric irregularities (Cherniak et al., 2018; Pi et al., 1997). ROTI, expressed in TECU/minute units, is calculated as the standard deviation of *N* values of *ROT*:

$$ROTI(t) = \sqrt{\frac{1}{N}\sum_{i=t-N}^{t}\left(ROT(i) - \overline{ROT}\right)^2} \quad (3)$$

In this study, the *ROTI* is calculated every 5 min in the case of 30-s measurements and 1 min in the case of 1-s measurements, which translates into *N* values of 10 and 60, respectively (with ROT being the average value calculated over the same periods). To derive oscillational features of TIDs, high-pass or band-pass filtering of VTEC can be used. Previous studies used moving average (Borries et al., 2023; Ferreira et al., 2020; Zakharenkova et al., 2016), polynomial fits (Ding et al., 2007; Habarulema et al., 2015; Nykiel et al., 2017), or other estimations of background TEC or trends (Hernández-Pajares et al., 2006). All these methods give similar results without any significant differences. It also has no effect if the ambiguities of phase measurements are determined or just uncalibrated VTEC is taken into account. To extract the *VTEC* variability, we used moving average with a 15-min and 60-min window size:

$$\Delta TEC(t) = \frac{1}{T_{15}}\sum_{i=t-0.5T_{15}}^{t+0.5T_{15}} VTEC(t) - \frac{1}{T_{60}}\sum_{i=t-0.5T_{60}}^{t+0.5T_{60}} VTEC(t) \quad (4)$$

TEC anomaly (ΔTEC) is calculated as a difference between a moving average with a 15-min and 60-min window size. T_{15} and T_{60} are the number of observations for each window size, which are 15-min/Δt and 60-min/Δt, respectively.

In our study, we used 30-s GPS phase observations derived from 350 stations belonging to the EUREF GNSS Permanent Network (EPN). *ROT*, *ROTI*, and ΔTEC parameters were calculated for each satellite-receiver link. We use an ionospheric single layer model with an altitude of 350 km. For *VTEC* estimation, we used phase-to-code alignment and satellite differential code biases (DCB) derived from the Center for Orbit Determination in Europe (CODE). Receivers' DCB's were estimated using methodology introduced by Brunini and Azpilicueta (2010). The results of the calculations were the values for each ionospheric pierce point (the intersection of the signal with the ionospheric layer at 350 km in altitude), which are distributed non-uniformly. Therefore, we used the inverse distance weighting method to create a regular grid with a spatial resolution of 0.2°.

2.2. EISCAT UHF and ESR Radars

The European Incoherent Scatter (EISCAT) UHF radar system (930 MHz) located at Tromsø (69.58°N, 19.21°E), Norway, was continuously operated during two experiment campaigns between 19 and 25 March 2023. At 08–20 UT, the radar was operated in a field-aligned geometry with an elevation/azimuth angle of 77.8°/189.20°. At 20–08 UT, the radar was operated in the EISCAT Common Program 2 (CP2) mode, also called beam-swinging mode. The radar beam is rotated between four pointing directions with a rotation cycle of 6 min. In Longyearbyen (79.15°N, 16.02°E) on Svalbard, Norway, the EISCAT Svalbard Radar (ESR, 500 MHz) was also operated nearly continuously from 20 to 25 March 2023. The receiver dish with a diameter of 42 m was pointed in a fixed direction along the local magnetic field with an elevation of 81.6°. For more information on the different EISCAT radar modes and geometries, see Tjulin (2021). The EISCAT UHF radar measurement data are available from the Madrigal database. The time resolution of the data shown in this study is 1 min to probe the altitude variation of electron and ion parameters.

2.3. Solar Wind and CME Data

We use data from the WIND spacecraft orbiting the Lagrange point 1 (L1 point) for the solar wind study. Magnetic field data is obtained from the Magnetic Field Investigation (MFI) instrument.The plasma parameters

(velocity, density, and temperature of the solar wind ions) are from the solar wind experiment (SWE) instrument. The WIND spacecraft data from 21 to 25 March 2023, were downloaded from the Automated Multi Dataset Analysis system (AMDA) and Coordinated Data Analysis Web (CDAWeb) of NASA. The information related to the Coronal Mass Ejection (CME) events of 20 March 2023, was collected from the LASCO (Large Angle and Spectrometric Coronagraph Experiment) instrument on board the SOHO (Solar and Heliospheric Observatory) mission. To describe the above CME events, we also use the real-time space weather information and simulation results from the Space Weather Database Of Notifications, Knowledge, Information (DONKI).

2.4. IMAGE Equivalent Currents

The International Monitor for Auroral Geomagnetic Effects (IMAGE) is a chain of magnetometers located in the European region sector, which allows for the monitoring of ground magnetic disturbances generated due to the ionospheric currents. The measurements are then projected to the ionospheric plane, and as a result, the so-called IMAGE Equivalent Currents (IEC) are obtained. The IEC corresponds to the horizontal equivalent ionospheric current associated with the magnetometer measurements. It is important to highlight, however, that the actual ionospheric currents would correspond to a combination of field-aligned and horizontal currents. At high latitudes, however, one can safely assume that IEC are approximately equal to the divergence-free horizontal part of the actual ionospheric current. The curl-free part of the ionospheric horizontal current, together with associated field-aligned current, are not detected by ground-based magnetometers (Vanhamäki & Juusola, 2020). The IEC is generated by the Finnish Meteorological Institute (FMI), and it provides valuable information on ionospheric electrodynamics and magnetosphere-ionosphere coupling (Tanskanen, 2009).

2.5. Defense Meteorological Satellite Program (DMSP)

The Defense Meteorological Satellite Program (DMSP) satellites F16 A, F17 A, and F18 a orbit at an altitude of around 840 km, with an inclination of 98.9°and a nominal period of 101 min. Their payloads include the Special Sensor J (SSJ) instruments which make it possible to obtain information on the precipitating auroral particles. The SSJ has been supporting different research products, such as auroral boundary identification and field-aligned currents. Since auroral particle precipitation plays a significant role in the energy input from the solar wind into the Earth's magnetosphere-ionosphere-thermosphere (MIT) systems, observing the features of the precipitating spectra can be a valuable source of information for the understanding of this energy transfer process (Redmon et al., 2017).

3. Observations

3.1. Overview of the Geomagnetic Storm on March 23–24, 2023

On 23 March 2023, the Earth witnessed one of the biggest storms of the 21st century (24th with Kp up to 8). According to NOAA Space Weather Scales, the event was recorded as the first G4-level severe geomagnetic storm of 2023 and the current solar cycle. According to DONKI, the geomagnetic storm on 23 March was associated with two CMEs released on 20 March at 02:41 and 14:42 UT. In the SOHO/LASCO CME catalog, the first one is classified as a partial halo CME with an apparent speed of 424 km/s, while the second one is classified as a halo CME with a speed of about 727 km/s. Since the CME released at 02:41 UT is classified as poor event, we consider the effects of the CME which was released at 14:42 UT for further discussion.

Figure 1 displays the solar wind data observed at WIND spacecraft upstream from the Earth for the period from 21 to 25 March 2023. The left panels show the magnetic field components (B_x, B_y, and B_z) in GSE coordinates and 1-hr disturbance storm time *Dst* in nT. The right panels depict density, ram pressure, flow speed, solar wind plasma beta, and Kp index, respectively. The solar wind speed data shows the presence of a fast solar wind stream ($|V_x| > 500$ kms^{-1}).

After 06:00 UT on 23 March, a rapid decrease in the Dst index is observed indicating that the ring current is growing and a magnetic storm is progressing. As marked (orange vertical line) in Figure 1, an ICME 1 and 2 were was observed by WIND at 05:54 UT on 24 March according to HELIO4CAST. The data also displays the structure of solar wind where the ICME has a magnetic cloud (MC) between 13:30 UT on 23 March and 07:14 UT on 24 March. The magnetic obstacle is the region followed by the sheath, with a less dense and colder structure

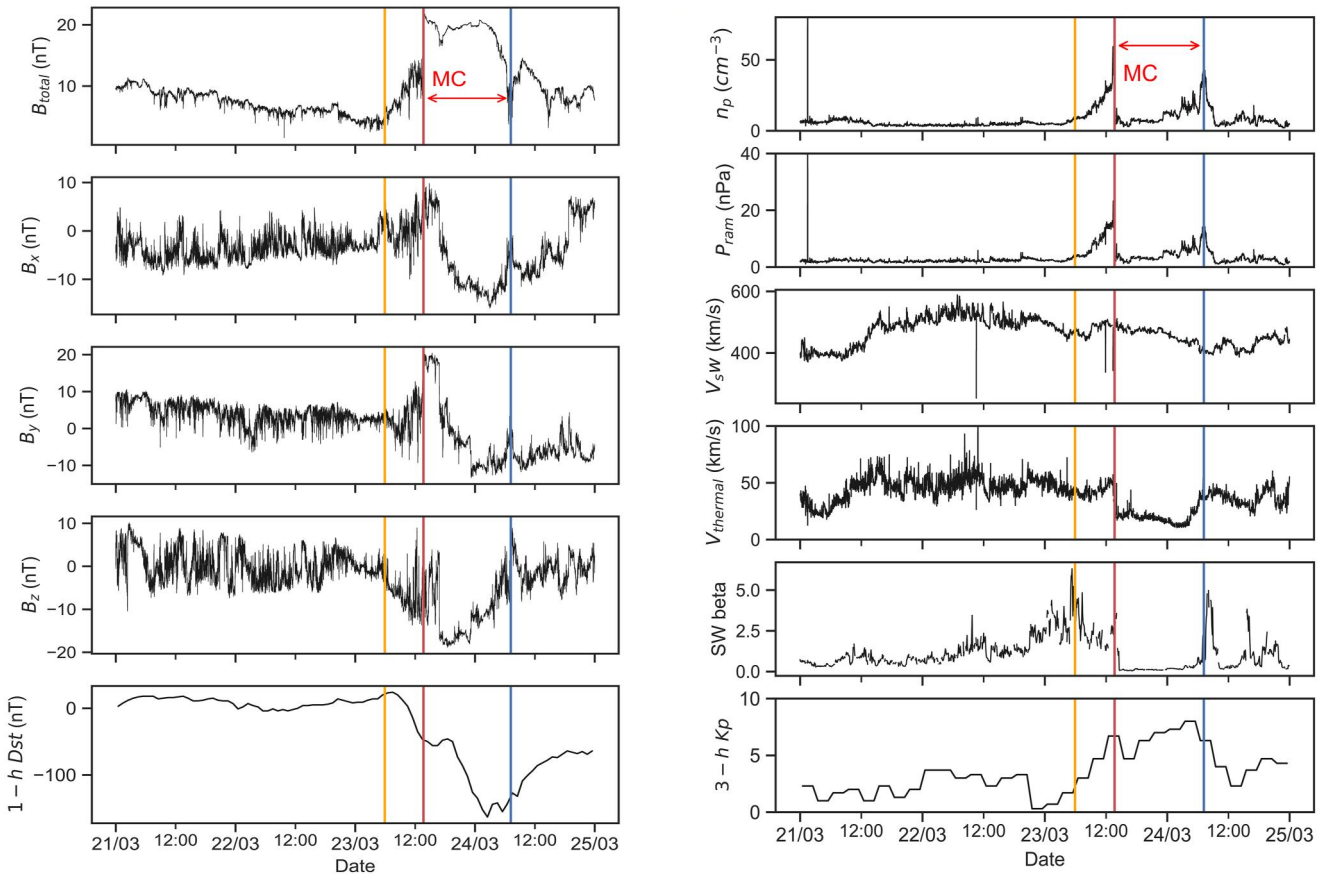

Figure 1. WIND data observed between 21 and 25 March. The left panel shows total magnetic field (B_{total}), components (B_x, B_y, B_z) in GSE coordinates, and the Disturbance Storm Time (Dst) index. The right panel displays ion density (n_p), ram pressure, solar wind flow speed V_{sw}, plasma beta, and Kp index. The orange, red, and blue vertical lines indicate the start of the ICME arrival time (05:54 UT), start time of the observed magnetic cloud (MC) and the end time of MC, respectively.

with an enhanced magnetic field with a flux rope structure (Nieves-Chinchilla et al., 2018, 2019), which is clearly visible in the data.

Figure 2 (left panel) shows the predicted magnetic field lines based on the methods by Tasnim et al. (2018, 2019) superposed on the maps of the radial velocity for the period from 21 to 25 March 2023, with the above-mentioned ICME and magnetic cloud. The field events strongly affect the ICME lines and display bidirectional field

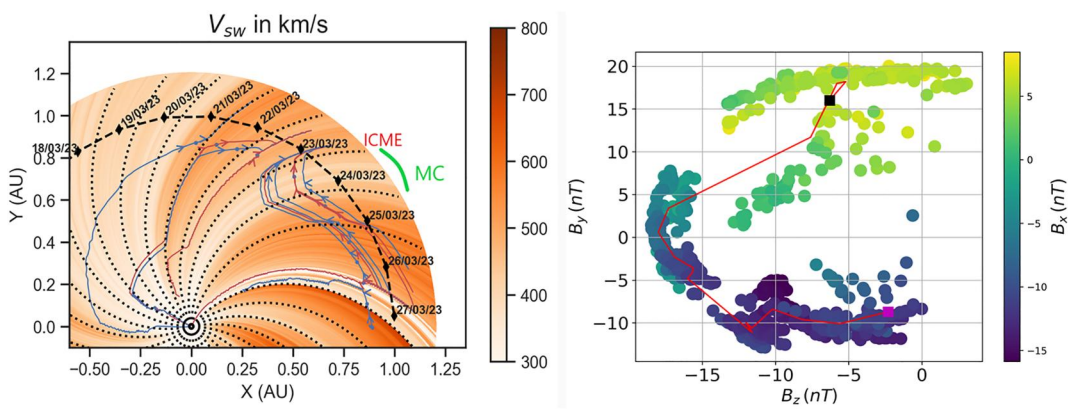

Figure 2. (Left panel) Predicted magnetic field lines from 19 to 27 March 2023 near Earth. (Right-panel) Variation of B_y with B_z for the period while magnetic obstacle was observed between 13:30 UT on 23 March and 07:14 UT on 24 March.

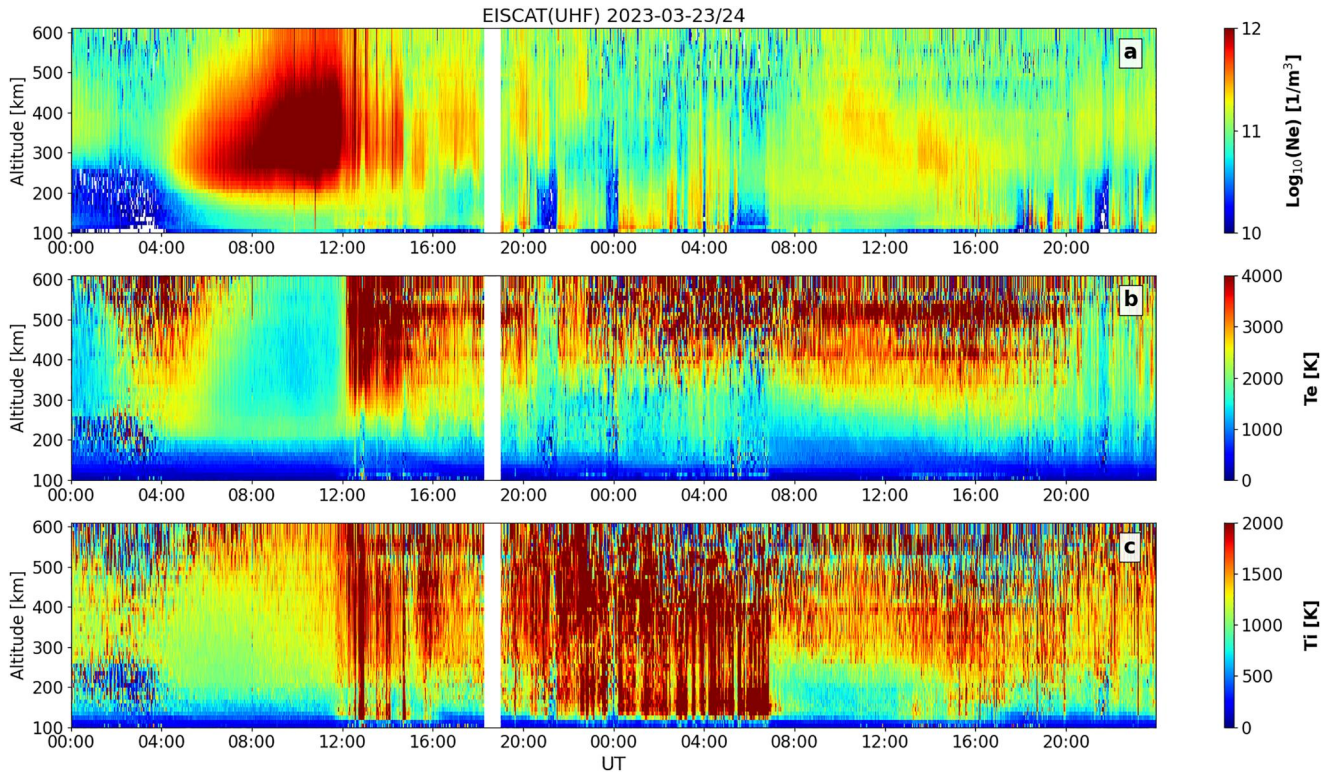

Figure 3. EISCAT UHF radar observation on 23–24 March, 2023. The color-coded profile of (a) electron density (b) electron temperature (c) ion temperature from 100 to 600 km altitudes. The data gap between 18:15 and 19:00 UT is shown by the white area.

orientations (i.e., the field lines close to MC and ICME are going inward and then outward). This local field line inversion portion (the bundle of field lines) on 23 and 24 March corresponds to the time when the ICME was observed near Earth. Note that the magnetohydrodynamic (MHD) model presented by Tasnim et al. (2018) assumes that the solar wind properties vary in the radial and longitudinal directions as a fixed pattern that rotates with the Sun past Earth. Although the model does not render the transients line interplanetary CMEs, we see sudden changes and complex magnetic structures when a CME is present in the solar wind observation and it provides us with the scope of the magnetic field lines for the chosen event of the geomagnetic storm observed on 24 March 2023.

We employ the approach used by Nieves-Chinchilla et al. (2019) and use the 1-min resolution of WIND data to briefly analyze the magnetic field configuration of the interplanetary magnetic field (IMF). The right panel of Figure 2 depicts the variation B_y with B_z for the period when the magnetic cloud is observed, where color represents the B_x in GSE components. It displays the magnetic hodogram of the GSE components B_y and B_z. A line (red) using hourly OMNIWeb data is overplotted. The start and end of the period are marked using black and magenta squares, respectively. In the $z-y$ plane, the magnetic field vectors experience a 180° rotation, which indicates a flux rope configuration.

3.2. EISCAT Observations of Ionospheric Density and Temperature in the Auroral and Polar Cap Regions

Figure 3 shows the color-coded plot of electron density (Ne), electron temperature (Te) and ion temperature (Ti) measurements as a function of altitude and time along the field line derived from the EISCAT UHF radar measurements in the auroral zone from 00:00 UT on 23 March to 24:00 UT on 24 March 2023. The time resolution is 1 min. The data covers the altitude range from 100 to 600 km. All three parameters Ne, Te and Ti show abrupt changes from around 11:41 UT, which is more clearly seen in the intersection at 300 km altitude as calculated as a deviation from the quiet-time reference values at 11:00 UT in Figure 5. In the day-time, the electron density started to generally decrease, accompanied by occasional sudden enhancements over background

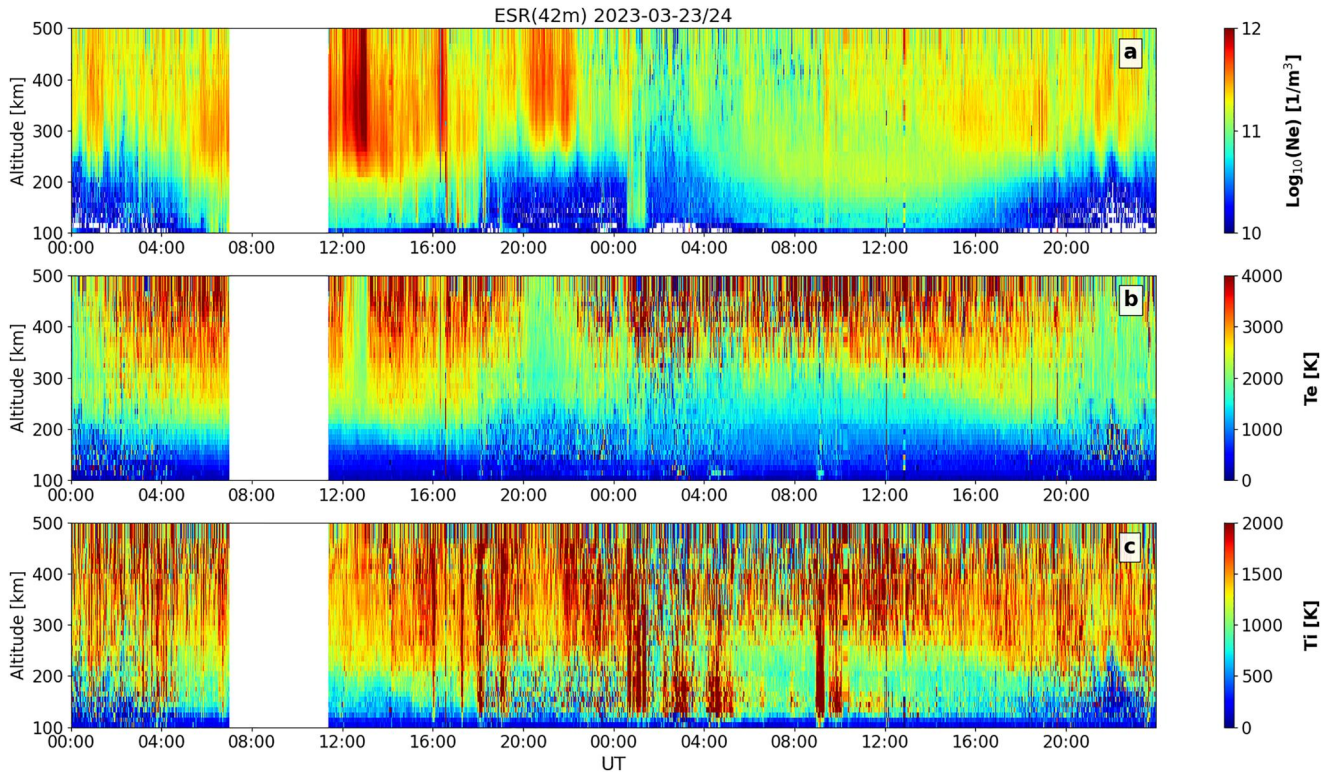

Figure 4. Similar to Figure 3, but from EISCAT Svalbard 42m radar observation on 23–24 March, 2023. (a) electron density (b) electron temperature (c) ion temperature from 100 to 500 km altitudes. The data gap between 07:00 and 11:24 UT is shown by the white area.

density while the electron and ion temperature are observed to be significantly enhanced from the quiet values. At 12:00 UT, Ne is decreased by 53% while Te and Ti are increased by 135% and 115%, respectively. The largest impacts of the storm until 13:00 UT are found for Ne at 12:58 UT (85%), for Te at 12:35 UT (225%), and for Te at 12:53 UT (274%).

In the day-time, the variation of electron density results from a combination of storm-induced sudden decrease/increases and a slower decrease due to daily variations toward the sunset. EISCAT data shows that the sudden electron density decrease and increase are generally associated with the periods of electron and ion heating in the day-time. The sudden increase of electron density seen at 100 km altitude suggests the occurrence of precipitating electrons down to the E-region. The heating of electrons is found above 200 km altitude and the most significant enhancements are found above 300 km. The heating of ions, on the other hand, is observed down to 100 km or below and occurred more abruptly than the electron heating.

In the night-time, the enhancements of electron density due to precipitation particles are more frequently found than in the day-time. The electron heating occurred mostly at the time of electron density enhancement, but the altitude of electron heating is found mainly above 400 km which is higher than the heating altitudes of the day-time. In contrast, ion heating occurred at a much larger altitude range than electrons. The ion temperature of higher than 2,000 K is observed between 100 and 600 km altitudes. This strong ion heating continued to around 07:00 UT on the following day where the temperature levels go down near the pre-storm levels with an elevated altitude of 300 km. In the night-time, the periods of continued ion heating are generally longer than those of electrons. Figure 3 shows that electron precipitations are often accompanied by electron and ion heating but ion heating can be found without electron density enhancements.

Figure 4 shows the electron density, temperature and ion temperature measurements from the EISCAT Svalbard radar in a color-coded format similar to Figure 3. Here, the altitude range is shown from 100 to 500 km. Despite the data gap in the morning period on 23 March, discontinuous variations of electron density are found around 12:00 UT. The largest electron density values in the day-time can be found between 12:50 and 13:05 UT without significant electron heating. We find that density enhancements due to precipitation events are also not always

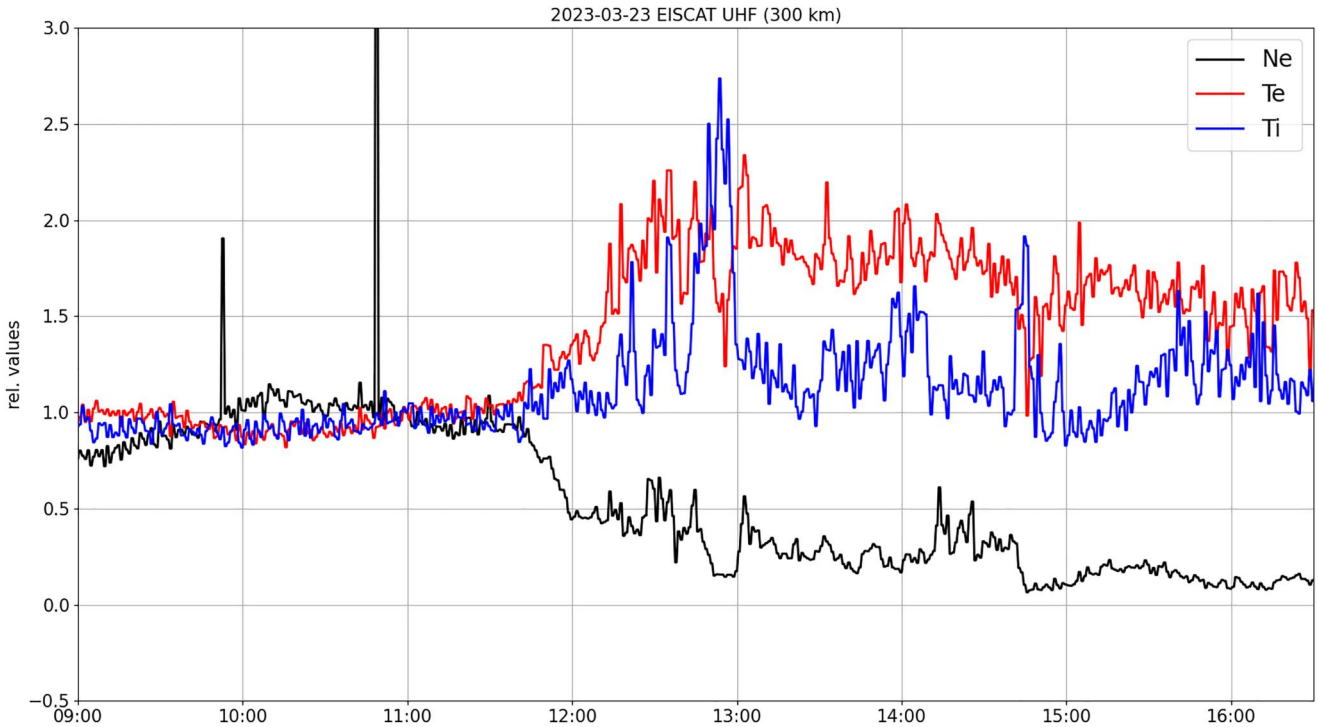

Figure 5. An intersection of EISCAT parameters from Figure 3 (Ne - electron density, Te - electron temperature, and Ti - ion temperature) at a 300 km altitude around the beginning of the geomagnetic storm on 23 March 2023.

accompanied by significant electron and ion heating also in the night-time. The largest electron density enhancements in the night time are found at around 21 UT with no electron heating but less ion heating than the vicinity hours. During the day-time, electron heating is observed down to 200 km altitudes. The electron heating altitude is elevated to 300 km altitude at night-time and also on the following day. The lowest altitudes of ion heating can be found between 200 and 100 km both in day- and night-time.

On 24 March, we find that the background electron density level is significantly reduced for both EISCAT locations. This can be seen over the occasional density enhancements due to precipitations. Electron and ion heating are continuously observed throughout the day both in the auroral zone and polar cap region, but with less enhanced temperature than on the previous day. This reduction of electron density is even more evident when compared to the pre-storm period. The UHF radar data shows that the F-region peak density at 11:00 UT on 23 March is 1.5×10^{12} at a 300 km altitude while at this height the electron density is 1.9×10^{11} at 11:00 UT on 24 March (87% decrease). The peak density in the F-region on the 24th is 2.2×10^{11} at a 390 km altitude (86% decrease).

3.3. GNSS TEC Observation of LSTID Propagation and Background Density

Figure 6 shows the GNSS-derived *VTEC* in the form of the latitude-time plot (along the meridian 15°E) for three consecutive days between 22 March (the day before the storm) and 24 March 2023. The results show that the VTEC value increased significantly for all latitudes during the storm. For a latitude of about 35°N, the maximum values were about 84 TECU between 12:00 and 13:00 UT. In contrast, for latitude 70°N around 11:00 UT, *VTEC* values were 56 TECU. Compared to the day before the storm, we see a marked increase in *VTEC*, which in some areas was almost 100% (Figure 10). This is especially true for the night hours between 23 and 24 March and areas in higher latitudes. At the same time, between 13:00 and 17:00 on 24 March, there are areas above 60°N where the VTEC values were lower by about 10 TECU, 50% of the *VTEC* value of the previous day. Joule heating may have caused this effect, which resulted in plasma depletion in the F region and consequently the *VTEC* trough. This effect is visible in the following hours, where *VTEC* depletion is propagated to lower latitudes. Generation of LSTIDs near the large gradients at the VTEC trough borders has been previously reported (Borries et al., 2017). On the day after the storm on 24 March, there is an apparent decrease in the concentration of electrons compared

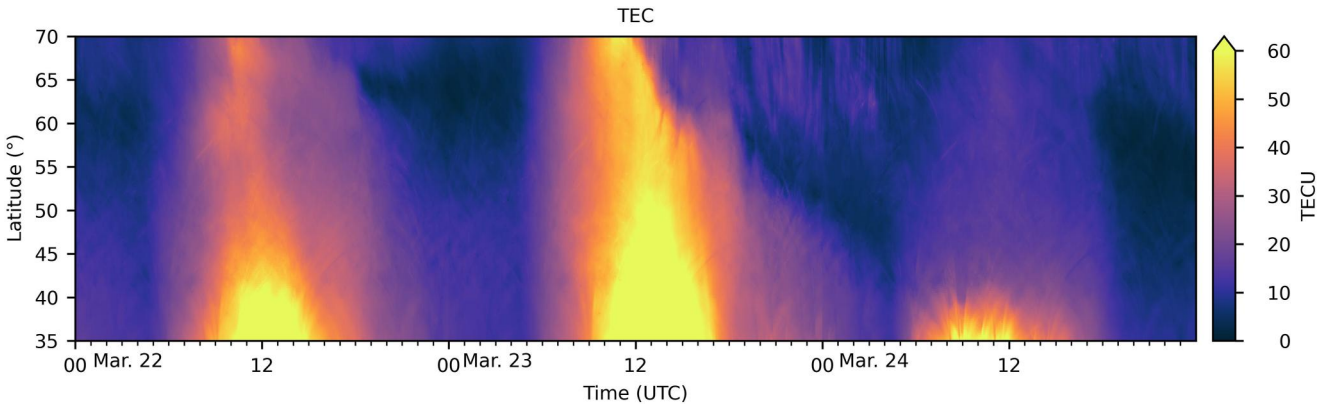

Figure 6. Latitude versus time plots centered at 15°E of Total Electron Content (TEC) from 22 March 2023 (00:00 UT) to 24 March 2023 (23:59 UT).

to the day of the storm and the day before. For most of the area, *VTEC* did not exceed 30 TECU (except for areas below 40°N where *VTEC* reached a maximum of 60 TECU). Compared to the day before the storm, differences even reached 30 TECU, which was a change of up to −80%.

To investigate the propagation of LSTIDs, we estimated Δ*TEC* according to Equation 4. The Δ*TEC* maps for 23 March 2023 during the day-time and night-time are shown in Figure 7. During the day, clear signatures of TID propagation from high to middle and lower latitudes were visible with a width covering the entire analyzed area. These southward-propagating TIDs had an amplitude of about 1 TECU and wavelength of about 1,200–1,300 km. During the night, significant, temporary, and rapid changes in Δ*TEC* caused by particle precipitations are seen in the auroral region. In the middle latitude, LSTIDs are characterized by smaller amplitude (about 0.6 TECU) and also in wavelength (about 700 km) ranges. An animation of Δ*TEC* changes over Europe between 23 March, 11:00 UTC and 24 March, 12:00 UTC has been attached as Supporting Information S1.

More detailed views of LSTID propagation in Δ*TEC* together with *ROTI* and *ROT* are presented in the form of latitude-time plots centered at 15°E (Figure 8). In Figure 8, while propagations of LSTIDs are seen as a diagonal structure over time in Δ*TEC* and *ROT*, TEC disturbances due to particle precipitation at high latitudes are seen especially clearly as the scale of 1 [TEC/min] in the *ROTI* plot. These *ROTI* disturbances in the high latitudes correspond to rapidly changing TEC as seen in *ROT*. Figure 8 shows that the day-time LSTIDs on 23 March originated from beyond 70°N and propagated down to southern Europe below 35°N while the night-time LSTIDs are observed to have originated in the (extended) auroral zone, which can be represented by disturbed *ROTI*.

We derive the propagation velocity of LSTIDs at a longitude of 15°E in Figure 9. From Figures 8 and 9, we focus on the LSTIDs that propagated over the middle latitudes (lower than 50°N), and analyze three types of observed LSTIDs: (I) on 23 March before 12 UT with an amplitude around 1 TECU and velocity about 1,100 m/s (Figure 9) with the source further north beyond the range of available GNSS data; (II) between 13 and 17 UT with different velocities between 550 and 750 m/s and an amplitude about 1 TECU, which were observed to be propagating from the inside or from the border of the auroral oval; (III) between 20 UT on 23 March and 2 UT on 24 March with a smaller amplitude (about 0.25 TECU) and velocity between 700 and 900 m/s, which were probably caused by large *VTEC* gradients at the boundary of the *VTEC* trough. Apart from this, numerous TIDs with different velocities and amplitudes are seen in the region of the auroral oval. The EISCAT radar measurements (Figures 3 and 4) generally show the occurrence of electron and ion heating during the generation of these LSTIDs. Despite the data gap in the EISCAT ESR observation time, Figure 4 indicates the existence of electron heating near the expected generation of type (I) LSTID near 11 UT on 23 March. Both at Svalbard and Tromsø, the longer electron heating periods in larger altitudes are observed during the day-time type (II) LSTIDs, while the ion heating in longer periods and a larger altitude range are found in night-time, which correspond to type (III) LSTIDs in Figure 8.

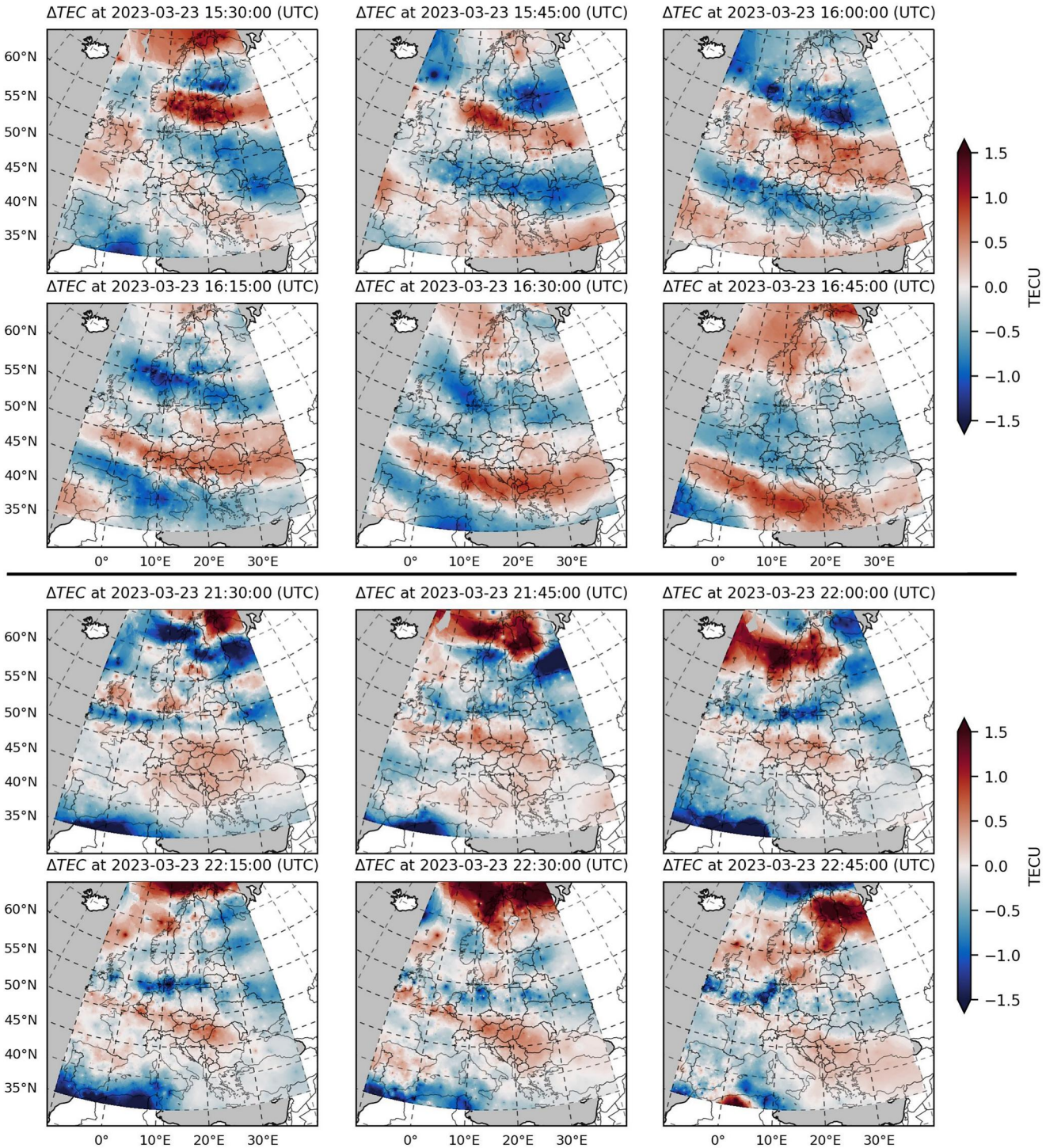

Figure 7. GNSS TEC anomaly (Δ*TEC*) observations over the European sector during the day-time (top) and the night-time (bottom). Δ*TEC* shows a snapshot of the propagation of an LSTID. Results derived from GNSS stations belonging to the EUREF GNSS Permanent Network (EPN).

4. Discussion

We have shown that the simultaneous and continuous measurements of EISCAT radars and GNSS TEC detected the generation and propagation of LSTIDs associated with the ionospheric disturbances in the auroral and polar cap regions on 23–24 March, 2023. We further analyze the EISCAT data to derive the wave signatures and

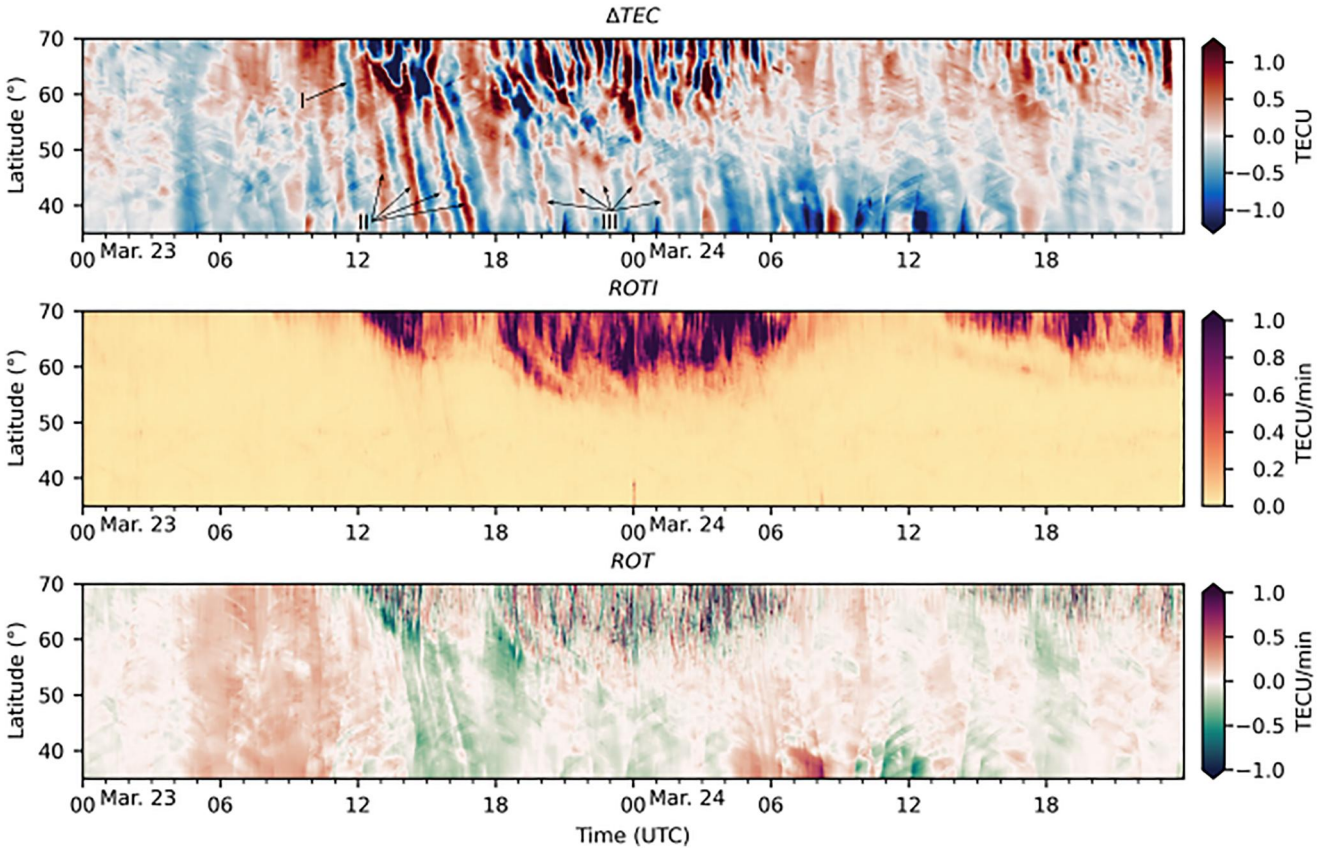

Figure 8. Latitude versus time plots centered at 15°E of Total Electron Content (TEC) variations from 23 March 2023 (00:00 UT) to 24 March 2023 (23:59 UT). First panel: TEC anomalies (ΔTEC) estimated using a moving average band-pass filter with 15- and 60-min periods. Second panel: rate of TEC index (ROTI). Third panel: rate of TEC (ROT).

primary energy deposition sources in the source region with comparison to other estimate methods from a physical model and other observations.

4.1. Wave Signatures in EISCAT Electron Density

The signature of atmospheric gravity waves and associated TIDs can be detected in EISCAT electron measurements by applying appropriate filters (Günzkofer et al., 2023; van de Kamp et al., 2014; Vlasov et al., 2011). While previous works focused mainly on using this method on MSTIDs, the extraction of wave features of LSTID wave features is possible given a long enough measurement period and an appropriate selection of filters. Here, we use an application of moving average filters as the most straight forward approach. The EISCAT electron density measurements from 23 to 24 March have been filtered with two moving averages with window lengths of $T_1 = 3$ hr and $T_2 = 1$ hr. By subtracting the filtered electron density variations from each other, oscillation periods between T_1 and T_2 are emphasized.

Figure 11 shows the filtered electron density measured with the EISCAT UHF radar. Wave signatures related to the LSTIDs on the scale of $\sim 4 \times 10^{10}[\mathrm{m}^{-3}]$ can be detected at about 100–200 km altitude the two nights following the geomagnetic storm. Note that, when integrated over a few hundred kilometers along the radar beam direction, these fluctuation levels of electron density become nearly 1 TECU which agree well with the GNSS TEC derived amplitude of LSTIDs (Figures 8 and 7). The LSTID wave period during both nights following the storm can be estimated from Figure 11 as ~75 min. The periods of these wave structures also agree with the TEC anomalies shown in Figures 8 and 9 at high latitudes. The EISCAT electron density measurements are therefore, a combination of storm-induced background variation and small-scale fluctuation related to LSTIDs. The time and altitude of these LSTIDs suggests the forcing from the particle precipitation energy deposition.

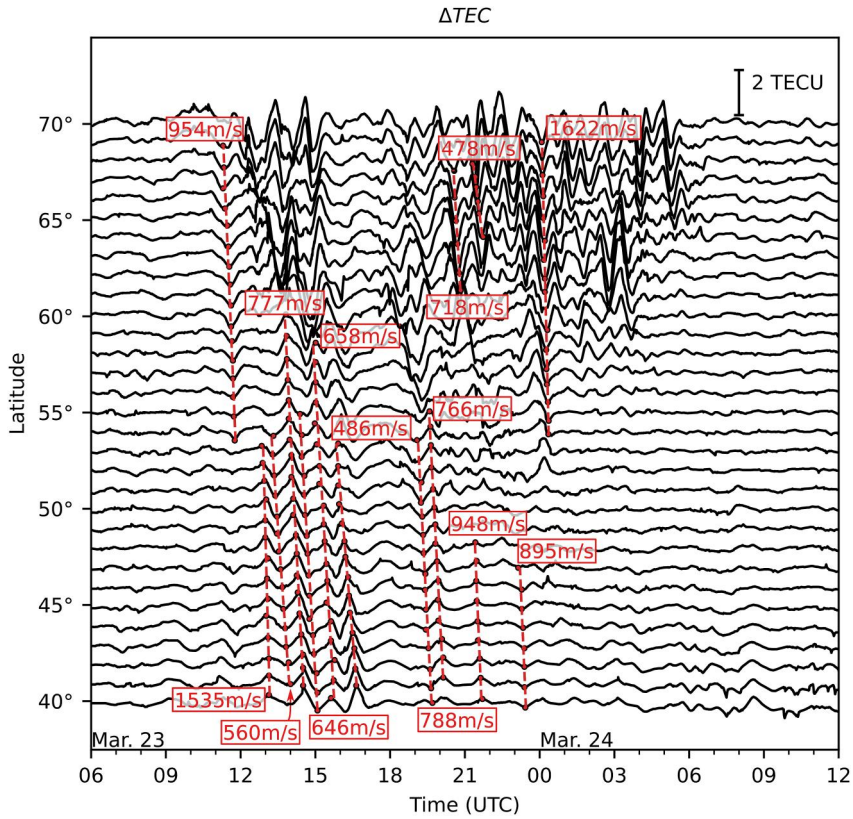

Figure 9. Profiles of the TEC anomalies at a longitude of 15°E. Each line represents a separate profile plotted every 1°from 40°N to 60°N. Dashed red lines represent the wave structure trajectory.

4.2. Energy Inputs From Joule Heating and Particle Precipitations Derived From EISCAT Data

The LSTIDs observed in Figure 11 are induced due to storm energy deposition in the thermosphere-ionosphere system. The two major energy deposition mechanisms are Joule heating and particle precipitation. Here, we estimate both the Joule heating rate Q_J and the particle precipitation energy deposition rate Q_P from EISCAT measurements with the method described by Vickrey et al. (1982) in order to determine the primary energy source for the observed LSTIDs. In this section, we first summarize the methods to calculate heating rates from EISCAT measurements and present the obtained heating rates during and after the March 2023 geomagnetic storm.

The energy deposition from particle precipitation Q_P can be estimated from EISCAT measurements of the electron density N_e. The heating power can be estimated as

$$Q_P = 5.6 \cdot 10^{-6} \int \sigma_{eff}(h) \cdot N_e(h)^2 \mathrm{d}h \quad [\mathrm{erg\ cm^{-2}\ s^{-1}}], \tag{5}$$

where $\sigma_{eff}(h) = 2.5 \cdot 10^{-6} \exp(-h/h_0)$ is the altitude-dependent effective recombination coefficient in $\mathrm{cm^3\ s^{-1}}$ units with the reference altitude $h_0 = 51.2$ km (Vickrey et al., 1982). N_e is applied in units of reciprocal cube centimeters and the altitude in km units. The relation in Equation 5 can only be assumed under certain conditions which limits the integration altitude range to 85 km $< h <$ 160 km (Vickrey et al., 1982). We calculate the particle precipitation heating rates from EISCAT measurements in Tromsø and on Svalbard.

The Joule heating is generated by the collisions between neutrals and charged particles moving in the direction of electric fields in the ionosphere. The Joule heating rate Q_J can only be calculated from EISCAT measurements if three-dimensional(3D) ion velocity vectors can be derived.This is possible if the radar is operated in the beam-swinging mode (see Section 2.2). Therefore, Joule heating rates are only available for the EISCAT Tromsø data and also only at night times from 20 to 08 UT. 3D ion velocity vectors are derived from the beam-aligned ion

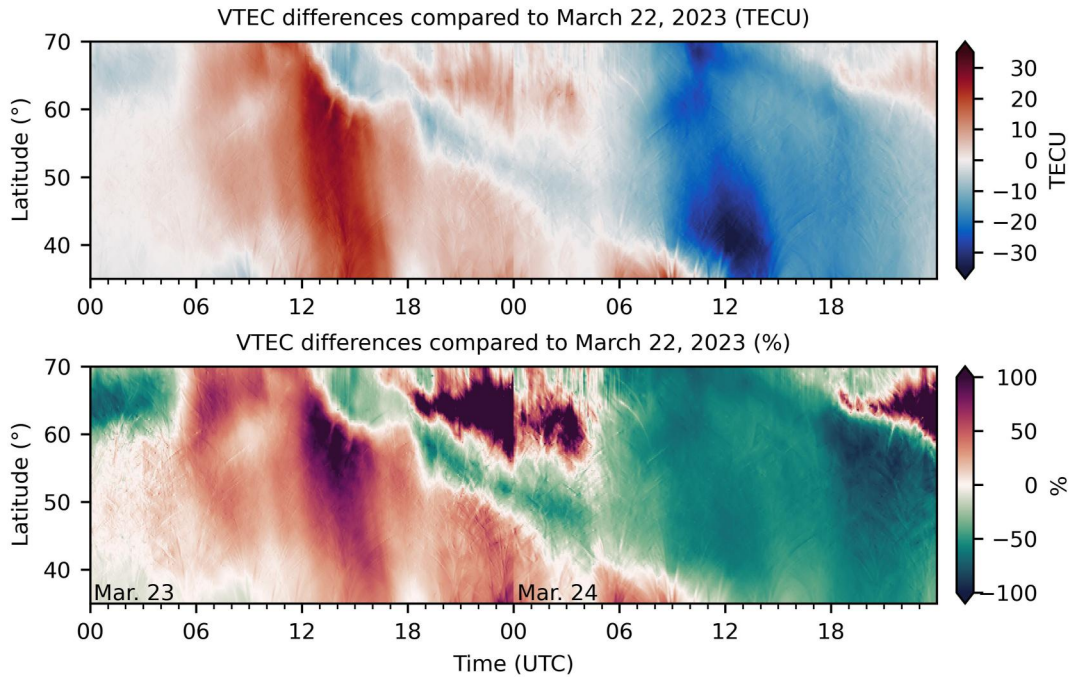

Figure 10. Latitude-time plots of TEC differences centered at 15°E from 23 March 2023 (00:00 UT) to 24 March 2023 (23:59 UT) with reference to the day before the storm – 22 March. The top panel presents differences in TECU, while the bottom panel shows the percentage change in TEC compared to the day before the storm.

velocity measurements by applying the stochastic inversion method described in Nygrén et al. (2011). Neglecting the impact of the neutral wind, which can be done for storm time conditions (Banks, 1977), the Joule heating rate is given as (Kavanagh et al., 2022; Vickrey et al., 1982)

$$Q_J = \Sigma_P \cdot E_\perp^2, \tag{6}$$

where the Pedersen conductance Σ_P is the height-integrated Pedersen conductivity which can be estimated from the EISCAT measurements. For better comparison, 85 km < h < 160 km is chosen, to be equivalent to the particle precipitation integration range. $E_\perp$ is the electric field component perpendicular to the magnetic field and can be

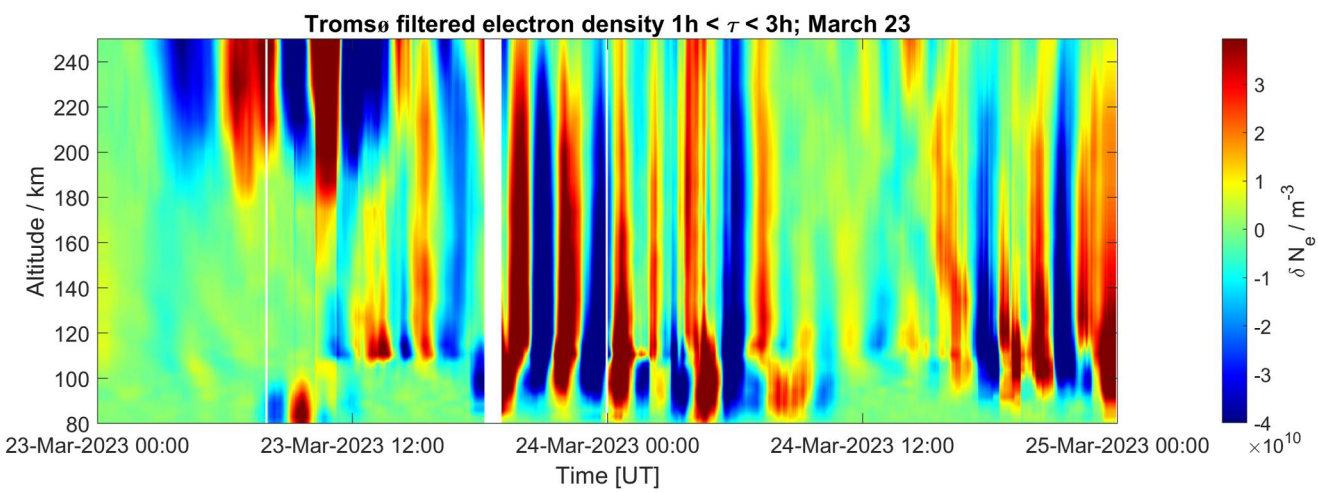

Figure 11. EISCAT Tromsø electron density filtered with two moving averages with window lengths T_1 = 3 hr and T_2 = 1 hr. Wave signatures are found for both day-time and night-time LSTIDs during 23–24 March, 2023.

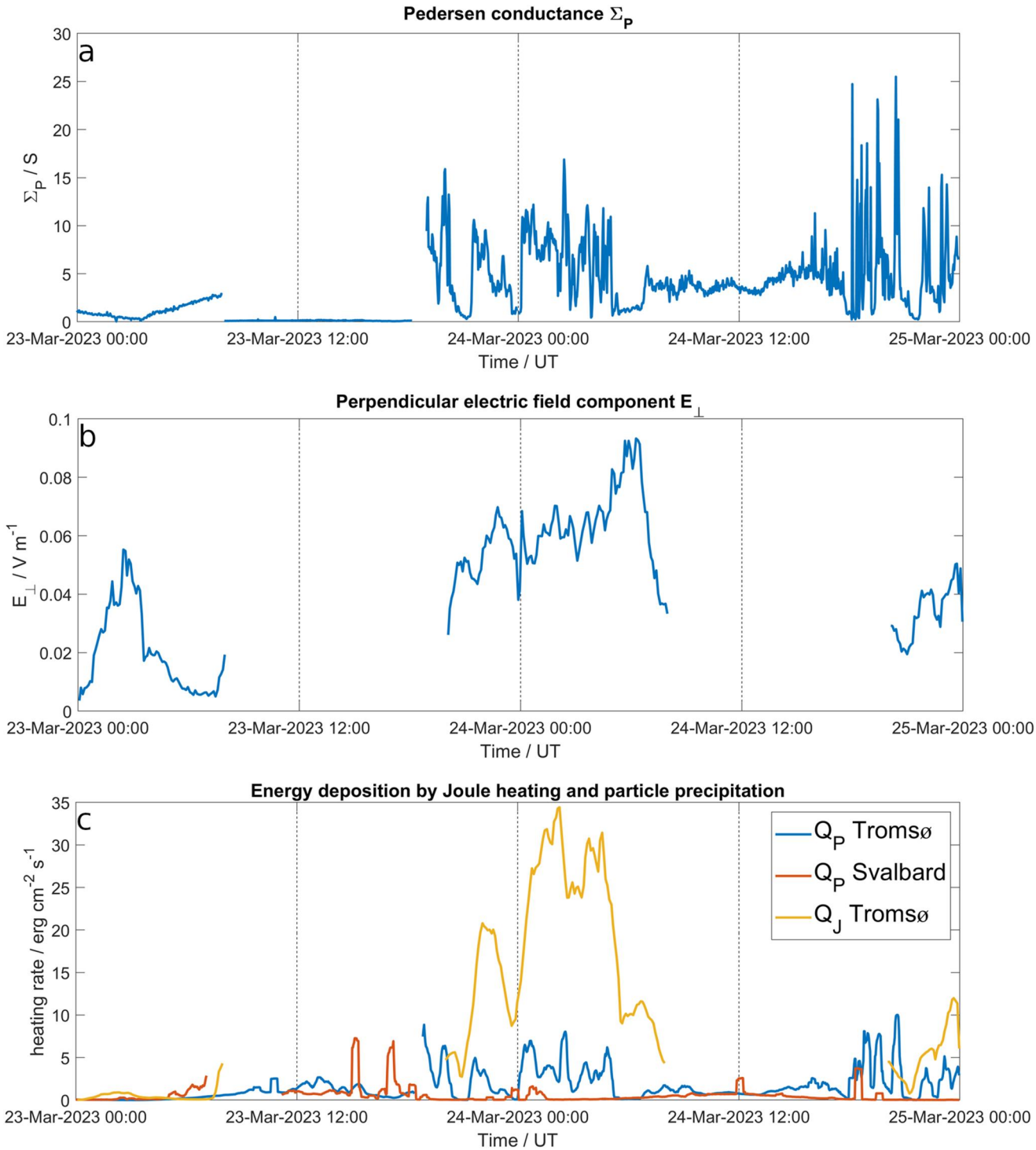

Figure 12. (a) Pedersen conductance Σ_P and (b) electric field component perpendicular to the Earth's magnetic field $E_\perp$ at Tromsø. (c) Joule heating and particle precipitation heating rates for 23–24 March at 85–160 km altitude. Q_P is given as a 20 min moving average and Q_J as 1 hour moving average.

calculated from the 3D ion velocity vector v_i and the magnetic field B, which is taken from the International Geomagnetic Reference Field (IGRF) (Thébault et al., 2015). The electric field is calculated at a 300 km altitude, where the ion drift equation $E_\perp = -v_i \times B$ holds. $E_\perp$ scales linearly with the increasing magnetic field strength at lower altitudes. The Pedersen conductance and the perpendicular electric field component are plotted in Figures 12a and 12b.

Figure 12c shows the energy deposition rates due to particle precipitation Q_P (Tromsø and Svalbard) and Joule dissipation Q_J (Tromsø) at 85−160 km altitude on 23–25 March. During the night following the geomagnetic storm on 23 March, the Joule heating rate is significantly increased and reaches the maximum values > 30 erg cm^{-2} s^{-1}. The particle precipitation rate Q_P in Tromsø is also increased during the two nights following the geomagnetic storm on 23 March. We note that Q_P and Q_J reach similar values during the second night after the storm with maximum values of ∼10 erg cm^{-2} s^{-1}. The increased night-time heating rates coincide with the LSTIDs detected in EISCAT measurements in Figure 11. The particle precipitation heating over Svalbard is generally lower than over Tromsø, although it reaches similar peak values shortly after the storm onset and clearly before the Tromsø Q_P maximum. This early heating at latitudes in the cusp region can explain the generation of LSTIDs observed before night-time on 23 March. A recent experimental study using auroral imagers and TEC shows that day-time LSTIDs are driven in the polar cusp by both soft electron precipitation and Joule heating (Nishimura et al., 2020). Our energy deposition estimate of two mechanisms from IS radar measurements of ionospheric density and temperature also shows that these two mechanisms acted as a time-varying energy source for the observed day-side LSTIDs during the day-time on 23–24 March 2023. It is challenging to isolate various processes which actively participate in the generation of LSTIDs. At high latitudes, electric fields may play an active role in the triggering as well as horizontal propagation of TIDs. Such electric field oscillations were previously indicated during MSTID occurrence (Kelley et al., 2023). Therefore, we examined the presence of significant ion velocity oscillation in the EISCAT measurements. The estimated line-of-sight ion velocities show no significant oscillation signatures inside the nighttime TID wave front bands at 100 km altitude where the nighttime electron density oscillations were largest (Figure 11). At higher altitudes, the line-of-sight ion velocity shows fluctuations which implies the presence of electric fields within the TID band. These fluctuations seem to accompany the electron density oscillation at 19:00 UT on 23 March with a delay (not shown), which cannot be fully determined due to the data gap. Such ion velocity fluctuations have been previously reported as a common feature of the TID (e.g., Vlasov et al., 2011). In order to complement EISCAT radar measurements, we compare our results with a larger-scale energy deposition from Joule heating from geomagnetic data and in-situ measurements of particle precipitation from DMSP satellites in the next section.

4.3. Regional and Global Estimates of Joule Heating

Figure 13a shows the Ionospheric Equivalent Currents (IEC) obtained from the IMAGE magnetometers network. An increase of the eastward IEC between 12 and 15 UT on 23 March reaches values of around 670 A/km. During this period, a displacement of the IEC from 70°N down to 65°N is observed. In the evening, the westward IEC intensifies and a clear displacement from around 70°down to 58°N is observed until midnight. Afterward, the westward IEC moves back toward north, reaching a magnitude of about −2,000 A/km shortly after 0 UT on 24 March, reaching back to 70°N at around 5 UT. On 24 March, at about 15 UT, an increase on the eastward IEC reaches a maximum of 570 A/km at 15:35 UT. From 15 UT to 19 UT, the displacement of the enhanced eastward IEC from 68°N to about 64°N is visible. Based on the maximum (or minimum) observed at each latitude, one can estimate the velocity of each displacement. This displacement occurs at a velocity of approximately 80 and 34 m/s for the eastward IECs and around 177 m/s for the westward one. The decreased level of the IEC and IE index (Figure 13b) around 18 UT on 23 March also corresponds to the absence of LSTID generation in the same period (see e.g., Figure 9). General agreement between the occurrence of LSTIDs and the increased level of auroral activity, electrojet and the Joule heating due to the dissipation of currents estimated by IEC was also found for a large magnetic storm (Ferreira et al., 2020).

To estimate Joule heating over the hemisphere, this study uses the Space Weather Modeling Framework (SWMF) model (version 20180525) which uses high-performance Block Adaptive Tree Solar-Wind Roe Upwind Scheme (BATS-RUS) code (e.g., Tóth et al., 2012). The Joule dissipation rate is calculated by CCMC as Wdiss in W/m^2 (computed as $\frac{J^2\sigma_P}{\sigma_P^2+\sigma_H^2}$). Solar wind input data is taken from OMNI. The input parameter for radio flux 10.7 cm is given as 157 for the model, the average daily value between start and end date of the run. Figure 14 shows the global integrated Joule heating for the northern Hemisphere during 22–27 March, 2023. The intensification of the integrated Joule heating corresponds to the storm main phase and the beginning of its recovery phase. The BATS-RUS result generally agrees with the Joule heating estimate from EISCAT data (Figure 12) as both results show that local peak values of Joule heating are found before and after the midnight on 24 March. Figure 14 also shows the occurrence of enhanced Joule heating in the afternoon of 23 March, where the EISCAT data is not available for the estimation of Joule heating.

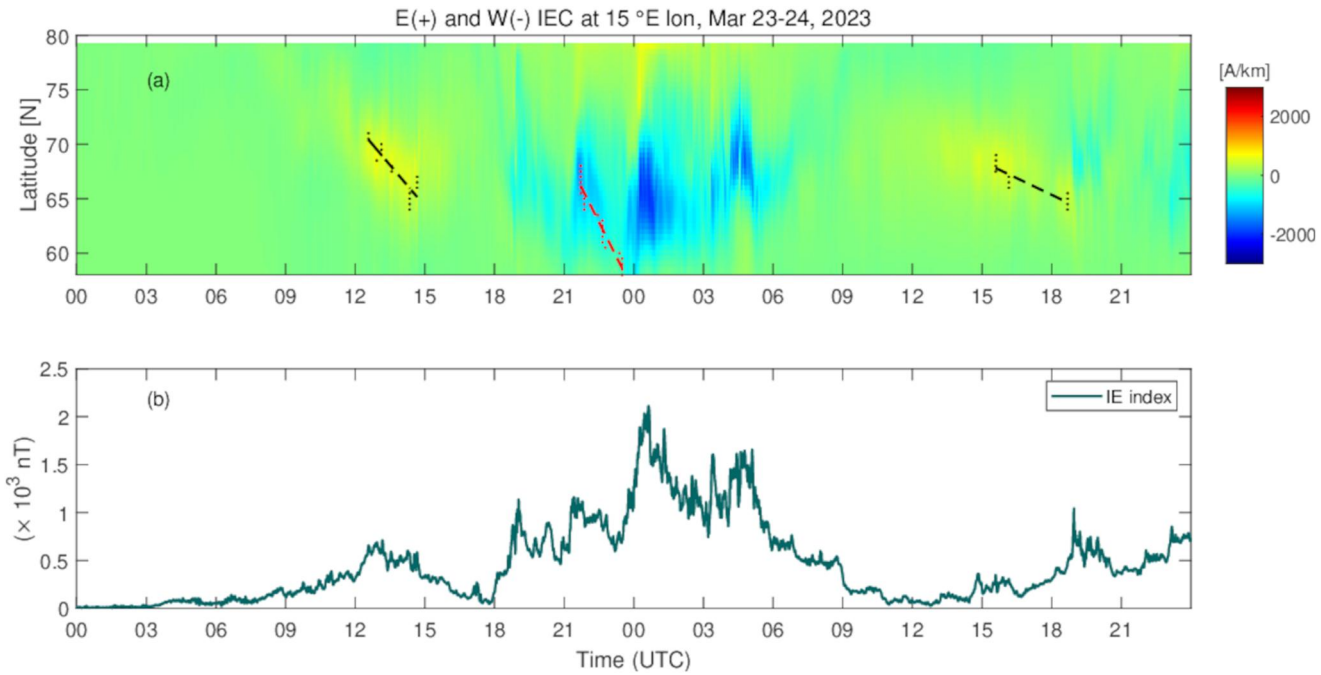

Figure 13. (a) Eastward and westward IMAGE ionospheric equivalent currents (IEC) at 15°E for 23–24 March, 2023. Black and red dots indicate the points for the linear fitting to estimate the velocities of east and west IEC displacements, respectively. The black (red) dots correspond to the maximum (minimum) IEC at each latitude. The fitting results for the eastward and westward IEC's are indicated by the black and red dashed-lines, respectively; (b) IMAGE IE index registered on 23–24 March, 2023.

4.4. Particle Precipitations From DMSP Data

The particle precipitations derived from DMSP satellite are considered for the satellite passages within the region 40–80°N latitude and 10–45°E longitude. Figure 15, upper row, presents the coordinates of some of the passages under these conditions. One can note that two passages are available for 23 March, and six passages are available for the following day. Figure 15, second row, presents the integrated electron (orange curve) and ion (green curve) energy fluxes. One can observe an increased precipitation during the satellite passages. Vertical dashed black lines are included to allow for better visualization of the lower latitudinal limit of such fluxed enhancements, which can help improve the interpretation of the particle precipitation impacts on the generation of the LSTIDs excited during the period. The lowest latitude can be observed on 24 March for the first passages of satellites

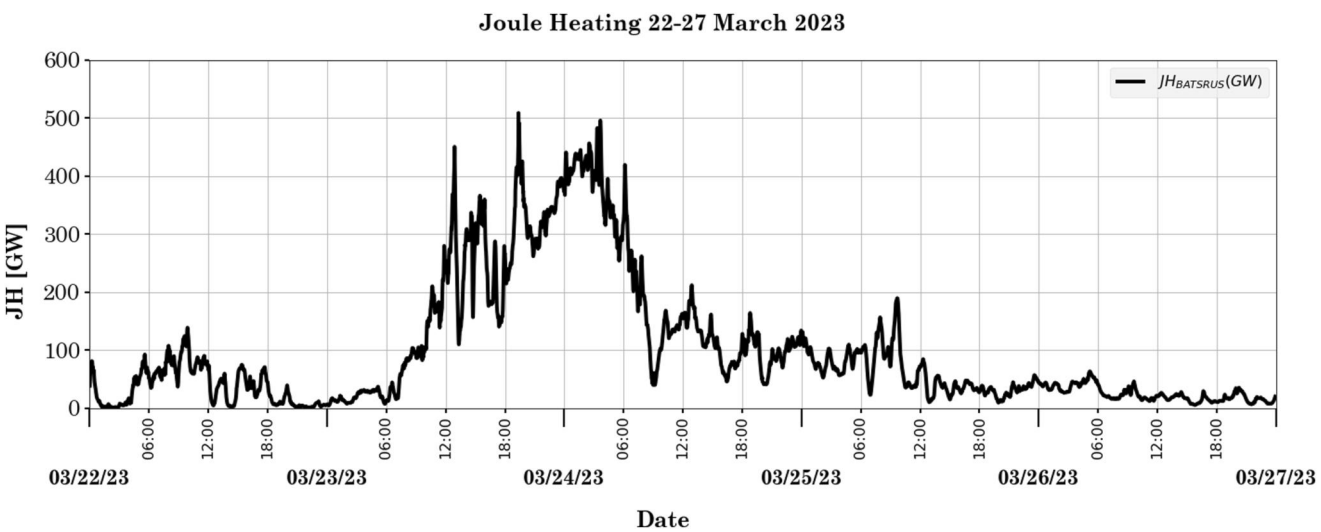

Figure 14. Global integrated Joule heating for Northern Hemisphere from SWMF/BATSRUS model output for 22–27 March, 2023.

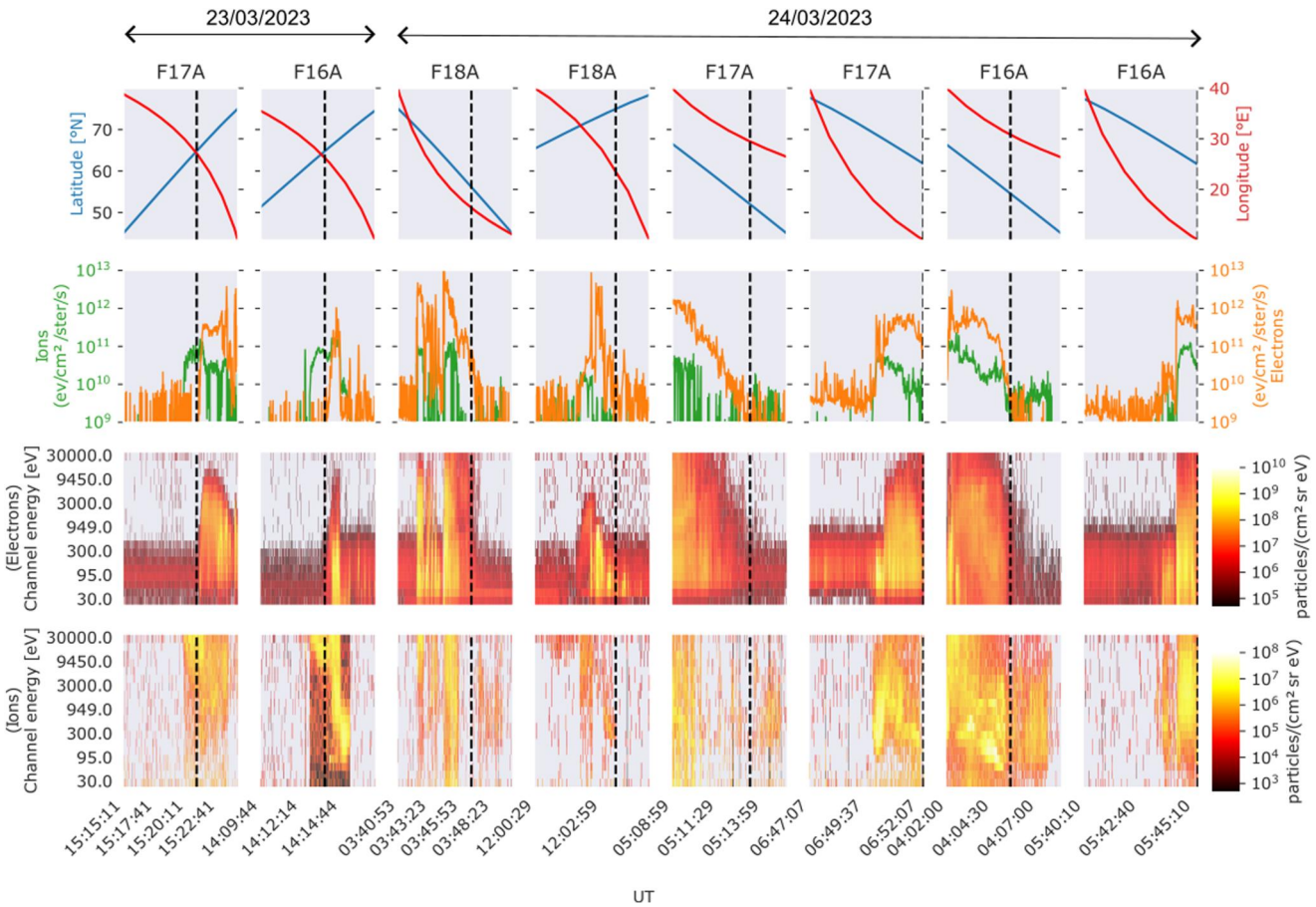

Figure 15. Selected DMSP passages over Europe for the 23 (left) and 24 (right) March, respectively. First panel: Geographic coordinates of the satellite during the passage (vertical projection to the ground). Second panel: Integrated electron/ion energy flux. Third panel: Differential electron energy flux. Fourth panel: Differential ion energy flux.

F16A, F17A and F18A reaching around 55°N, indicating an increased precipitation of particles in this region. From the DMSP measurements, one can observe that integrated electron and ion energy fluxes are reached in the order of 10^{13} and 10^{11} ev/cm^2/ster/s, respectively. Figure 15, third row, presents the differential electron energy flux measured at different energy levels (from 30 up to 30,000 eV). It shows that an increase in the number of detected particles is observed in almost all channels for all the passages. The enhancement energy levels reached above 9,450 eV for the most of the passages. . For the differential ion energy flux, Figure 15 fourth row, one can observe an increase in the number of particles mainly for energy levels above 95 eV. The comparison of the integrated energy fluxes of electrons and ions shows that the former dominates for the satellite passages investigated in this work.

4.5. Sources and Propagation Characteristics of LSTIDs

In order to analyze the source mechanisms of the observed LSTIDs, the observed disturbances are classified into three types, indicated in Figure 8 (upper panel) as I, II, and III. Figures 8 and 9 show a single high-speed TID reaching 70°N before 12 UT. The estimated propagation velocity for this disturbances is about 954 m/s, and it shows an amplitude of about 1 TECU at 60°N. According to the IEC presented in Figure 13a, an increase in the eastward electrojet before 12 UT is observed in the region around 75°N. Although this enhancement is not as strong as the one observed between 12 and 15 UT, it suggests an increased auroral activity at that region, which can contribute to the excitation of the TID mentioned above. This can be supported by the increased IE index observed in Figure 13b. The IE index is derived from the IMAGE magnetometers network (Tanskanen, 2009), and it is a commonly used index to assess the level of geomagnetic activity in the auroral region. Different from the other LSTIDs observed during this storm, the source region of the TID above is not visible in Figure 8 (upper

plot), suggesting that the auroral electrojets were located further north when compared to the other LSTIDs generated during this storm. Figure 14 shows increased Joule heating during the period. Unfortunately, no DMSP data is available to assess the level of particle precipitation for this period and region.

On 23 March, from 12 to 15 UT, different LSTIDs with speeds between 500 and 750 km/s are observed (see Figures 8 and 9). During this period, increased differential electron/ion energy fluxes on the 23rd are detected from the DMSP satellites F16A and F17A (see Figure 15), indicating enhanced particle precipitation at latitudes above 60°N, approximately, which also corresponds to the source region of the excited LSTIDs. Figure 13a shows increased eastward IEC observed during the period. The increased eastward electrojet is observed at the exact location of the increased ion/electron fluxes observed from DMSP measurements. These results suggest that the observed LSTIDs are closely related to both effects: particle precipitation and Joule heating due to the dissipation of currents. Although particle precipitation is not as effective as Joule heating at heating the whole high-latitude upper atmosphere, it may generate localized effects, such as increasing the ionospheric conductivity through the impact of ionization (Knipp et al., 2004, 2013). As a consequence, one can observe an enhancement of currents and the associated Joule heating. From Figure 10, one can observe a depletion on TEC at the source region of the observed LSTIDs. Such a TEC depletion in the source region of LSTIDs is considered to be related to thermospheric expansion due to Joule heating (Borries et al., 2017). As a result of such thermospheric expansion, heavier molecules (O_2 and N_2) are transported to higher altitudes where they contribute to the increase of the recombination rate, which is reflected by a lower level of TEC.

From 19 UT on the 23 March until 04 UT on 24 March, a set of LSTIDs is observed in middle latitude Europe. During this period, a significant increase in the geomagnetic auroral activity and Joule heating is observed in Figures 13b and 14. This is also the period when the irregularities observed in high-latitudes are mostly displaced to lower latitudes. The LSTIDs that propagated over the middle latitudes (lower than 50°N) during this period have smaller amplitudes when compared to the previous ones, and their source region is located further south. For this set of LSTIDs the source region shifts southwards with a velocity of about 50 [m/s] and is closely related to the depletion on the TEC presented on Figure 10. By analyzing Figure 13a, one can also note that the westward IEC during the period follows the expansion of the high latitude irregularities up to around midnight on 24 March. From midnight until 4 UT, the source region of the TIDs is located below 50°N. This is considerably further south of the location of the increased westward IEC and the irregularities observed at higher latitudes (Figure 8, second and third panels). The passages of DMSP satellite F16A at around 04 UT indicates increased particle precipitation at regions around 55°N. At the same time, the enhanced westward IEC is located further north (at around 65°N). By comparing Figures 8 and 10 one can observe that the source region of such LSTIDs follows the TEC depletion band, which moves from around 60°down to 45°N shown in Figure 10. This band of depleted TEC corresponds to the middle latitude ionospheric trough, which may shift during geomagnetic storms as a result of a strong compression of the plasmasphere (Borries et al., 2016; Yizengaw & Moldwin, 2005). Close to the midlatitude trough region, the occurrence of Subauroral Polarization Streams (SAPS) has been reported in different investigations (Kunduri et al., 2021; Zhang et al., 2022). SAPS corresponds to rapid westward plasma convection driven by a strong poleward electric field located at the equatorward boundary of the auroral oval in the dusk-midnight sector of the ionosphere during geomagnetically disturbed periods (Anderson et al., 1993; Guo et al., 2018). Such SAPS are associated with substantial ion flow, ion drag, and frictional heating in the upper atmosphere and may induce the occurrence of TIDs (Guo et al., 2018; Zhang et al., 2022). The increased Joule heating (shown in EISCAT data and SWMF/BATSRUS model) due to the dissipation of currents combined with the SAPS is considered contributor to the excitation of the observed night-time LSTIDs.

5. Conclusions

The geomagnetic storm on 23–24 March 2023 was triggered by two CMEs on 20 March and it generated large ionospheric disturbances over the European sector. We investigated day-time and night-time LSTIDs during the geomagnetic storm by using two EISCAT IS radars and GNSS TEC covering the whole European sector in order to study energy transfer in the ionosphere-thermosphere system that drives LSTIDs that propagated equatorwards to lower latitudes with velocities between around 500 and 1,600 [m/s]. Enhanced particle precipitation and auroral electrojets are observed in the source region of the LSTIDs. We focused on LSTIDs that propagated large distance to middle latitudes and studied the relative contribution of two energy sources that can drive LSTIDs: Joule heating and particle precipitation from IS radar data in the source region and models. At night-time, both EISCAT and the BATS-RUS model results show large energy inputs from Joule heating in the

auroral region with the peaks around the midnight between 23–24 March, which are considered to be the primary energy source for the observed LSTIDs. During the day-time, both particle precipitation and Joule heating can be comparable energy source for LSTIDs that are originated near the polar cap. The day-time LSTIDs have the highest amplitudes and are therefore most clearly identifiable in the propagation down over the middle latitudes. GNSS-ROT illustrates an expansion of auroral region and the LSTIDs can be also associated with the large density depletion region that may be caused by Joule heating.

We also found that both EISCAT and GNSS TEC shows that ionospheric density is significantly decreased by 50% on the following day and the density decrease expands down to the middle latitude as geomagnetic activity increases. This decrease of density (so-called negative storm effects) started in the high latitude and propagated with speeds of around 50 m/s. The negative effects on TEC (40–70°N) are most clearly seen after 08 UT on 24 March. During this negative storm phase, no clear LSTIDs are observed by our methods. The storm-induced atmospheric heating is suggested as the cause of the significant background density decrease.

This study demonstrated that combination of dense GNSS receiver network data and plasma parameters derived from incoherent scatter radar is an effective tool to better understand and characterize large-scale space weather events such as LSTIDs. We also showed that wave signatures in electron density can be also studied by IS radar data. This work presented one of rare case studies of LSTIDs with regard to their source energies and their propagation for an entire magnetic storm period. Future studies including higher rate GNSS receiver data and new ground radar missions are expected to contribute to investigate further details of generation mechanism of LSTIDs.

Data Availability Statement

The EISCAT data is accessible at https://portal.eiscat.se/schedule/. RINEX files from GNSS stations belonging to the EUREF Permanent GNSS Network (EPN) can be downloaded from: https://epncb.oma.be/_networkdata/data_access/. The IMAGE 2D Ionospheric Equivalent Currents data used in this study are accessible on the Zenodo repository (Nykiel et al., 2023). The DMSP SSJ data are accessible at CEDAR Madrigal database http://cedar.openmadrigal.org/. The HELIO4CAST data used in this study is accessible at https://helioforecast.space/icmecat/ICME_Wind_MOESTL_20230323_01. The SOHO/LASCO CME Catalog is available at https://cdaw.gsfc.nasa.gov/CME_list/. Simulation results have been provided by the Community Coordinated Modeling Center (CCMC) at Goddard Space Flight Center through their publicly available simulation services (https://ccmc.gsfc.nasa.gov). The AMDA data is accessible at https://amda.irap.omp.eu/. The DONKI tool is available at https://kauai.ccmc.gsfc.nasa.gov/DONKI/. The OMNIWeb data are available at https://omniweb.gsfc.nasa.gov.

Acknowledgments

GN acknowledges support from the Gdańsk University of Technology through the DEC-13/2022/IDUB/II.1/ AMERICIUM grant under the AMERICIUM — "Excellence Initiative - Research University" program. EISCAT is an international association supported by research organizations in China (CRIRP), Finland (SA), Japan (NIPR and ISEE), Norway (NFR), Sweden (VR), and the United Kingdom (UKRI). We acknowledge the Community Coordinated Modeling Center (CCMC) at Goddard Space Flight Center for the use of the Space Weather Database Of Notifications, Knowledge, Information (DONKI) tool. The SOHO/LASCO data used here are produced by a consortium of the Naval Research Laboratory (USA), Max-Planck-Institut fuer Aeronomie (Germany), Laboratoire d'Astronomie (France), and the University of Birmingham (UK). SOHO is a project of international cooperation between ESA and NASA. We also acknowledge the Wind/SWE electron

References

Anderson, P. C., Hanson, W. B., Heelis, R. A., Craven, J. D., Baker, D. N., & Frank, L. A. (1993). A proposed production model of rapid subauroral ion drifts and their relationship to substorm evolution. *Journal of Geophysical Research: Space Physics*, *98*(A4), 6069–6078. https://doi.org/10.1029/92JA01975

Banks, P. M. (1977). Observations of joule and particle heating in the auroral zone. *Journal of Atmospheric and Terrestrial Physics*, *39*(2), 179–193. https://doi.org/10.1016/0021-9169(77)90112-X

Borries, C., Ferreira, A. A., Nykiel, G., & Borges, R. A. (2023). A new index for statistical analyses and prediction of travelling ionospheric disturbances. *Journal of Atmospheric and Solar-Terrestrial Physics*, *247*, 106069. https://doi.org/10.1016/j.jastp.2023.106069

Borries, C., Jakowski, N., Kauristie, K., Amm, O., Mielich, J., & Kouba, D. (2017). On the dynamics of Large-scale Traveling Ionospheric Disturbances over Europe on 20 November 2003. *Journal of Geophysical Research: Space Physics*, *122*(1), 1199–1211. https://doi.org/10.1002/2016JA023050

Borries, C., Mahrous, A. M., Ellahouny, N. M., & Badeke, R. (2016). Multiple ionospheric perturbations during the Saint Patrick's Day storm 2015 in the European-African sector. *Journal of Geophysical Research: Space Physics*, *121*(11), 11333–11345. https://doi.org/10.1002/2016JA023178

Brunini, C., & Azpilicueta, F. (2010). GPS slant total electron content accuracy using the single layer model under different geomagnetic regions and ionospheric conditions. *Journal of Geodesy*, *84*(5), 293–304. https://doi.org/10.1007/s00190-010-0367-5

Cai, H. T., Yin, F., Ma, S. Y., & McCrea, I. W. (2011). Observations of AGW/TID propagation across the polar cap: A case study. *Annales Geophysicae*, *29*(8), 1355–1363. https://doi.org/10.5194/angeo-29-1355-2011

Cherniak, I., Krankowski, A., & Zakharenkova, I. (2018). ROTI maps: A new IGS ionospheric product characterizing the ionospheric irregularities occurrence. *GPS Solutions*, *22*(3), 69. https://doi.org/10.1007/s10291-018-0730-1

Ding, F., Wan, W., Liu, L., Afraimovich, E., Voeykov, S., & Perevalova, N. (2008). A statistical study of Large-scale Traveling Ionospheric Disturbances observed by GPS TEC during major magnetic storms over the years 2003–2005. *Journal of Geophysical Research*, *113*(A3). https://doi.org/10.1029/2008JA013037

Ding, F., Wan, W., Ning, B., & Wang, M. (2007). Large-scale Traveling Ionospheric Disturbances observed by GPS total electron content during the magnetic storm of 29–30 October 2003. *Journal of Geophysical Research*, *112*(A6). https://doi.org/10.1029/2006JA012013

instrument team and NASA/GSFC and the Principal Investigator R.P. Lepping for use of the Wind/MFI magnetogram data. We acknowledge use of NASA/GSFC's Space Physics Data Facility's OMNIWeb. We are grateful to the AMDA science analysis system provided by the Centre de Données de la Physique des Plasmas (CDPP) supported by CNRS, CNES, Observatoire de Paris and Université Paul Sabatier, Toulouse. The SWMF Model was developed by the Center for Space Environment Modeling at the University of Michigan. This work was carried out using the SWMF and BATS-R-US tools developed at the University of Michigan's Center for Space Environment Modeling (CSEM). The modeling tools described in this publication are available online through the University of Michigan for download and are available for use at the Community Coordinated Modeling Center (CCMC). We thank the institutes who maintain the IMAGE Magnetometer Array: Tromsø Geophysical Observatory of UiT the Arctic University of Norway (Norway), Finnish Meteorological Institute (Finland), Institute of Geophysics Polish Academy of Sciences (Poland), GFZ German Research Centre for Geosciences (Germany), Geological Survey of Sweden (Sweden), Swedish Institute of Space Physics (Sweden), Sodankylä Geophysical Observatory of the University of Oulu (Finland), DTU Technical University of Denmark (Denmark), and Science Institute of the University of Iceland (Iceland). The provisioning of data from AAL, GOT, HAS, NRA, VXJ, FKP, ROE, BFE, BOR, HOV, SCO, KUL, and NAQ is supported by the ESA contracts number 4000128139/19/D/CT as well as 4000138064/22/D/KS. The authors would like to thank Dr. Liisa Juusola for providing the IMAGE 2D Ionospheric Equivalent Currents data. We thank the DMSP, Boston College and CEDAR Madrigal teams for providing DMSP SSJ data. We also thank the EUREF Permanent GNSS Network (EPN) for providing GNSS RINEX files from permanent stations. The GNSS data were processed at the Academic Computer Centre in Gdansk. Open Access funding enabled and organized by Projekt DEAL.

Ferreira, A. A., Borries, C., Xiong, C., Borges, R. A., Mielich, J., & Kouba, D. (2020). Identification of potential precursors for the occurrence of Large-scale Traveling Ionospheric Disturbances in a case study during September 2017. *J. Space Weather Space Clim.*, *10*, 32. https://doi.org/10.1051/swsc/2020029

Günzkofer, F., Pokhotelov, D., Stober, G., Mann, I., Vadas, S. L., Becker, E., et al. (2023). Inferring neutral winds in the ionospheric transition region from atmospheric-gravity-wave traveling-ionospheric-disturbance (AGW-TID) observations with the EISCAT VHF radar and the Nordic Meteor Radar Cluster. *Annales Geophysicae*, *41*(2), 409–428. https://doi.org/10.5194/angeo-41-409-2023

Guo, J.-P., Deng, Y., Zhang, D.-H., Lu, Y., Sheng, C., & Zhang, S.-R. (2018). The effect of subauroral polarization streams on ionosphere and thermosphere during the 2015 St. Patrick's Day storm: Global ionosphere-thermosphere model simulations. *Journal of Geophysical Research: Space Physics*, *123*(3), 2241–2256. https://doi.org/10.1002/2017JA024781

Habarulema, J. B., Katamzi, Z. T., & Yizengaw, E. (2015). First observations of poleward Large-scale Traveling Ionospheric Disturbances over the African sector during geomagnetic storm conditions. *Journal of Geophysical Research: Space Physics*, *120*(8), 6914–6929. https://doi.org/10.1002/2015JA021066

Hernández-Pajares, M., Juan, J. M., & Sanz, J. (2006). Medium-scale traveling ionospheric disturbances affecting GPS measurements: Spatial and temporal analysis. *Journal of Geophysical Research: Space Physics*, *111*(A7). https://doi.org/10.1029/2005JA011474

Hocke, K., & Schlegel, K. (1996). A review of atmospheric gravity waves and travelling ionospheric disturbances: 1982–1995. *Annales Geophysicae*, *14*(9), 917–940. https://doi.org/10.1007/s00585-996-0917-6

Jacobsen, K. S., & Andalsvik, Y. L. (2016). Overview of the 2015 St. Patrick's Day storm and its consequences for RTK and PPP positioning in Norway. *Journal of Space Weather and Space Climate*, *6*, A9. https://doi.org/10.1051/swsc/2016004

Kavanagh, A. J., Ogawa, Y., & Woodfield, E. E. (2022). Two techniques for determining F-region ion velocities at meso-scales: Differences and impacts on joule heating. *Journal of Geophysical Research (Space Physics)*, *127*(6), e30062. https://doi.org/10.1029/2021JA030062

Kelley, I. J., Kunduri, B. S. R., Baker, J. B. H., Ruohoniemi, J. M., & Shepherd, S. G. (2023). Storm time electrified MSTIDs observed over mid-Latitude North America. *Journal of Geophysical Research (Space Physics)*, *128*(3), e2022JA031115. https://doi.org/10.1029/2022JA031115

Kirchengast, G., Hocke, K., & Schlegel, K. (1996). The gravity wave - TID relationship: Insight via theoretical model - EISCAT data comparison. *Journal of Atmospheric and Terrestrial Physics*, *58*(1), 233–243. https://doi.org/10.1016/0021-9169(95)00032-1

Knipp, D. J., Kilcommons, L., Hunt, J., Mlynczak, M., Pilipenko, V., Bowman, B., et al. (2013). Thermospheric damping response to sheath-enhanced geospace storms. *Geophysical Research Letters*, *40*(7), 1263–1266. https://doi.org/10.1002/grl.50197

Knipp, D. J., Tobiska, W. K., & Emery, B. A. (2004). Direct and indirect thermospheric heating sources for solar cycles 21-23. *Solar Physics*, *224*(1), 495–505. https://doi.org/10.1007/s11207-005-6393-4

Kunduri, B. S. R., Baker, J. B. H., Ruohoniemi, J. M., Coster, A. J., Vines, S. K., Anderson, B. J., et al. (2021). An examination of magnetosphere-ionosphere influences during a saps event. *Geophysical Research Letters*, *48*(19), 1–9. https://doi.org/10.1029/2021GL095751

Lyons, L. R., Nishimura, Y., Zhang, S.-R., Coster, A. J., Bhatt, A., Kendall, E., & Deng, Y. (2019). Identification of auroral zone activity driving large-scale traveling ionospheric disturbances. *Journal of Geophysical Research: Space Physics*, *124*(1), 700–714. https://doi.org/10.1029/2018JA025980

Ma, S. Y., Schlegel, K., & Xu, J. S. (1998). Case studies of the propagation characteristics of auroral TIDS with EISCAT CP2 data using maximum entropy cross-spectral analysis. *Annales Geophysicae*, *16*(2), 161–167. https://doi.org/10.1007/s00585-998-0161-3

Mannucci, A. J., Wilson, B. D., Yuan, D. N., Ho, C. H., Lindqwister, U. J., & Runge, T. F. (1998). A global mapping technique for gps-derived ionospheric total electron content measurements. *Radio Science*, *33*(3), 565–582. https://doi.org/10.1029/97RS02707

Marques, H. A., Marques, H. A. S., Aquino, M., Veettil, S. V., & Monico, J. a. F. G. (2018). Accuracy assessment of precise point positioning with multi-constellation gnss data under ionospheric scintillation effects. *J. Space Weather Space Clim.*, *8*, A15. https://doi.org/10.1051/swsc/2017043

Nieves-Chinchilla, T., Jian, L. K., Balmaceda, L., Vourlidas, A., dos Santos, L. F. G., & Szabo, A. (2019). Unraveling the internal magnetic field structure of the earth-directed interplanetary coronal mass ejections during 1995–2015. *Solar Physics*, *297*(7), 89. https://doi.org/10.1007/s11207-019-1477-8

Nieves-Chinchilla, T., Vourlidas, A., Raymond, J. C., Linton, M. G., Al-haddad, N., Savani, N. P., et al. (2018). Understanding the internal magnetic field configurations of ICMES using more than 20 years of wind observations. solar physics. *Solar Physics*, *293*(2), 25. https://doi.org/10.1007/s11207-018-1247-z

Nishimura, Y., Zhang, S. R., Lyons, L. R., Deng, Y., Coster, A. J., Moen, J. I., et al. (2020). Source region and propagation of dayside large-scale traveling ionospheric disturbances. *Geophysical Research Letters*, *47*(19), e2020GL089451. https://doi.org/10.1029/2020GL089451

Nygrén, T., Aikio, A. T., Kuula, R., & Voiculescu, M. (2011). Electric fields and neutral winds from monostatic incoherent scatter measurements by means of stochastic inversion. *Journal of Geophysical Research (Space Physics)*, *116*(A5), A05305. https://doi.org/10.1029/2010JA016347

Nykiel, G., Amaral Ferreira, A., Günzkofer, F., Iochem, P., Tasnim, S., & Sato, H. (2023). Large-scale traveling ionospheric disturbances over the European sector during the geomagnetic storm on March 23-24, 2023: Energy deposition in the source regions and the propagation characteristics. [Dataset]. Zenodo. https://doi.org/10.5281/zenodo.10390629

Nykiel, G., Zanimonskiy, Y. M., Yampolski, Y. M., & Figurski, M. (2017). Efficient usage of dense gnss networks in central europe for the visualization and investigation of ionospheric tec variations. *Sensors*, *17*(10), 2298. https://doi.org/10.3390/s17102298

Otsuka, Y., Shiokawa, K., Ogawa, T., & Wilkinson, P. (2004). Geomagnetic conjugate observations of medium-scale traveling ionospheric disturbances at midlatitude using all-sky airglow imagers. *Geophysical Research Letters*, *31*(15), L15803. https://doi.org/10.1029/2004GL020262

Pi, X., Mannucci, A. J., Lindqwister, U. J., & Ho, C. M. (1997). Monitoring of global ionospheric irregularities using the worldwide gps network. *Geophysical Research Letters*, *24*(18), 2283–2286. https://doi.org/10.1029/97GL02273

Poniatowski, M., & Nykiel, G. (2020). Degradation of kinematic ppp of gnss stations in central europe caused by medium-scale traveling ionospheric disturbances during the St. Patrick's day 2015 geomagnetic storm. *Remote Sensing*, *12*(21), 3582. https://doi.org/10.3390/rs12213582

Redmon, R. J., Denig, W. F., Kilcommons, L. M., & Knipp, D. J. (2017). New DMSP database of precipitating auroral electrons and ions. *Journal of Geophysical Research: Space Physics*, *112*(8), 9056–9067. https://doi.org/10.1002/2016JA023339

Richmond, A. D. (1978). Gravity wave generation, propagation, and dissipation in the thermosphere. *Journal of Geophysical Research: Space Physics*, *83*(A9), 4131–4145. https://doi.org/10.1029/JA083iA09p04131

Richmond, A. D. (1979). Large-amplitude gravity wave energy production and dissipation in the thermosphere. *Journal of Geophysical Research: Space Physics*, *84*(A5), 1880–1890. https://doi.org/10.1029/JA084iA05p01880

Schaer, S. (1999). *Mapping and predicting the earth's ionosphere using the global positioning system*. (PhD Thesis). University of Bern, Bern.

Shiokawa, K., Otsuka, Y., Tsugawa, T., Ogawa, T., Saito, A., Ohshima, K., et al. (2005). Geomagnetic conjugate observation of nighttime medium-scale and large-scale traveling ionospheric disturbances: FRONT3 campaign. *Journal of Geophysical Research (Space Physics)*, *110*(A5), A05303. https://doi.org/10.1029/2004JA010845

Tanskanen, E. I. (2009). A comprehensive high-throughput analysis of substorms observed by IMAGE magnetometer network: Years 1993–2003 examined. *Journal of Geophysical Research: Space Physics*, *114*(A5), 1–11. https://doi.org/10.1029/2008JA013682

Tasnim, S., Cairns, I. H., Li, B., & Wheatland, M. S. (2019). Mapping magnetic field lines for an accelerating solar wind. *Solar Physics*, *294*(11), 155. https://doi.org/10.1007/s11207-019-1541-4

Tasnim, S., Cairns, I. H., & Wheatland, M. S. (2018). A generalized equatorial model for the accelerating solar wind. *Journal of Geophysical Research*, *123*(2), 1061–1085. https://doi.org/10.1002/2017JA024532

Thébault, E., Finlay, C. C., Beggan, C. D., Alken, P., Aubert, J., Barrois, O., et al. (2015). International geomagnetic reference field: The 12th generation. *Earth Planets and Space*, *67*(1), 79. https://doi.org/10.1186/s40623-015-0228-9

Tjulin, A. (2021). *Eiscat experiments (Tech. Rep.)*. EISCAT Scientific Association.

Tóth, G., van der Holst, B., Sokolov, I. V., De Zeeuw, D. L., Gombosi, T. I., Fang, F., et al. (2012). Adaptive numerical algorithms in space weather modeling. *Journal of Computational Physics*, *231*(3), 870–903. https://doi.org/10.1016/j.jcp.2011.02.006

Tsugawa, T., Otsuka, Y., Coster, A. J., & Saito, A. (2007). Medium-scale traveling ionospheric disturbances detected with dense and wide TEC maps over North America. *Geophysical Research Letters*, *34*(22), L22101. https://doi.org/10.1029/2007GL031663

Tsugawa, T., Saito, A., & Otsuka, Y. (2004). A statistical study of large-scale traveling ionospheric disturbances using the GPS network in Japan. *Journal of Geophysical Research: Space Physics*, *109*(A6). https://doi.org/10.1029/2003JA010302

Tsunoda, R. T., & Cosgrove, R. B. (2001). Coupled electrodynamics in the nighttime midlatitude ionosphere. *Geophysical Research Letters*, *28*(22), 4171–4174. https://doi.org/10.1029/2001GL013245

van de Kamp, M., Pokhotelov, D., & Kauristie, K. (2014). TID characterised using joint effort of incoherent scatter radar and GPS. *Annales Geophysicae*, *32*(12), 1511–1532. https://doi.org/10.5194/angeo-32-1511-2014

Vanhamäki, H., & Juusola, L. (2020). *Introduction to spherical elementary current systems*. In M. W. Dunlop & L. Lühr (Eds.), *Ionospheirc multi-spacecraft analysis tools* (pp. 5–34). Springer Cham. https://doi.org/10.1007/978-3-030-26732-2

Vickrey, J. F., Vondrak, R. R., & Matthews, S. J. (1982). Energy deposition by precipitating particles and Joule dissipation in the auroral ionosphere. *Journal of Geophysical Research*, *87*(A7), 5184–5196. https://doi.org/10.1029/JA087iA07p05184

Vlasov, A., Kauristie, K., van de Kamp, M., Luntama, J. P., & Pogoreltsev, A. (2011). A study of traveling ionospheric disturbances and atmospheric gravity waves using EISCAT Svalbard Radar IPY-data. *Annales Geophysicae*, *29*(11), 2101–2116. https://doi.org/10.5194/angeo-29-2101-2011

Yizengaw, E., & Moldwin, M. B. (2005). The altitude extension of the mid-latitude trough and its correlation with plasmapause position. *Geophysical Research Letters*, *32*(L09105), 1–5. https://doi.org/10.1029/2005GL022854

Zakharenkova, I., Astafyeva, E., & Cherniak, I. (2016). Gps and glonass observations of large-scale traveling ionospheric disturbances during the 2015 St. Patrick's Day storm. *Journal of Geophysical Research: Space Physics*, *121*(12), 12138–12156. https://doi.org/10.1002/2016JA023332

Zhang, S.-R., Erickson, P. J., Coster, A. J., Rideout, W., Vierinen, J., Jonah, O., & Goncharenko, L. P. (2019). Subauroral and polar Traveling Ionospheric Disturbances during the 7–9 September 2017 storms. *Space Weather*, *17*(12), 1748–1764. https://doi.org/10.1029/2019SW002325

Zhang, S.-R., Nishimura, Y., Erickson, P. J., Aa, E., Kil, H., Deng, Y., et al. (2022). Traveling Ionospheric Disturbances in the vicinity of storm-enhanced density at midlatitudes. *Journal of Geophysical Research: Space Physics*, *127*(8), 1–22. https://doi.org/10.1029/2022JA030429